DEVELOPMENT OF PARTICLE RECONSTRUCTION IN THE T2K ND280 ELECTROMAGNETIC CALORIMETERS AND AN EARLY STUDY INTO NEUTRINO INDUCED CHARGED CURRENT SINGLE PION EVENTS

A Thesis in High Energy Physics

by

Thomas Maryon

MPhys

Submitted in partial fulfilment

of the requirements for the degree of

Doctor of Philosophy

June 2013

Department of Physics

Lancaster University

No part of this thesis has been previously submitted for the award of a higher degree.

Abstract

The T2K ND280 detector is used to characterise the beam of neutrinos travelling from J-PARC to the Super-Kamiokande detector before they have oscillated to other neutrino types. This thesis first details the physics of neutrino interactions and oscillations, then gives an introduction to the T2K experiment and ND280 detector. The author took a key role in developing the software for the ND280 so the software packages created to run and analyse all aspects of the experimental data are described. Particular attention is paid to the reconstruction of physics objects in the ND280's electromagnetic calorimeter, as this is where the author did a large part of his work. A track fitting tool for use with commissioning data is then described. This was developed to reconstruct straight tracks which provided data needed to tune calibration methods and monitor the progress of electromagnetic calorimeter commissioning in early 2010. An analysis is presented for the detection and classification of charged current single neutral pion events in the ND280. The aims of this short investigation were to ascertain whether the detector could make a precision measurement of the event and to try to provide understood events to help with calibration and early detector commissioning. All work included in this thesis was undertaken between summer 2007 and summer 2010.

Acknowledgments

For my mum and my wonderful wife.

With special thanks to all the folks at Lancaster for their support, especially Peter Ratoff and his infinite patience.

Table of Contents

List of Figures

Chapter 1

Introduction

The existence of neutrino mass and oscillation between flavours was the first experimentally verified particle physics phenomenon which cannot be explained through the Standard Model. These phenomena therefore warranted further investigation and the T2K experiment was designed to measure oscillations in neutrino flavour after a propagation distance, or baseline, of 295km. The source of neutrinos is a high flux neutrino beam adapted from an existing proton accelerator at J-PARC on the east coast of Japan. The J-PARC facility also houses the ND280 detector suite, a newly constructed near detector tasked with categorising the beam close to its source. In addition, the ND280 detector provides a means to investigate a number of important cross-sections. These cross sections give rise to significant backgrounds in the detection and classification of neutrino interactions, particularly through the decay of π^0 particles which are yet to be well categorised and can closely mirror a ν_e interaction. The far detector, which sits at the far end of baseline, is the previously constructed and very successful water Cherenkov detector Super-Kamiokande, which is situated in Kamioka close to the west coast of Japan.

The neutrinos produced in the T2K experiment are at an energy, direction and propagation distance that benefit the study of the mixing angles θ_{13} and θ_{23}. At the time of T2K's inception, the angle θ_{13} was of special interest to the neutrino physics community as it had yet to be measured and, if found to be non-zero, would allow the existence of a CP violating phase.

This thesis will pay special attention to the ND280 detector, its calorimetry and the measurement of π^0 interactions within the detector. This mirrors the author's involvement with the experiment between summer 2007 and summer 2010. The initial focus of the thesis, in chapter 2, will be understanding the physics and some of the history behind the discovery of neutrinos and their oscillations. This will provide some context for the studies detailed in the thesis and allow for an explanation of some of the physics investigated.

Chapter 3 will give a brief overview of the detector hardware used in the experiment. Special focus here will be given to the ND280 downstream electromagnetic calorimeter. This subdetector was constructed at Lancaster University as part of the UK's contribution to the ND280 detector. It also acted as a prototype for subsequent calorimetry modules in the ND280.

Much of the author's time working at Lancaster University was spent helping with the construction of the ND280's calorimetry and working on the software used to reconstruct physics objects within it. As such the next chapter, chapter 4, details the software used to run, reconstruct and analyse interactions within the ND280 detector. Special focus is given here to the reconstruction and analysis of events in the electromagnetic calorimeter. I then describe a short investigation into a first pass track-fitter program designed to pick out straight, MIP-like tracks. This was developed for use in the calibration of the ND280 calorimetry and was of particular importance during the commissioning of the calorimetry at J-PARC in early 2010. The penultimate chapter details a short investigation into the detection and classification of charged current π^0 events in a section of the ND280 detector. The aim of this early study was to first ascertain whether the detector could make a precision measurement of the events and then try to provide understood events to help with calibration and early detector commissioning. Finally I will conclude this thesis with a summary of the work done by the author and how this work fits in with the overall aim of the T2K experiment.

Chapter 2

Theory

2.1 Neutrino History

Neutrinos are neutral very low mass particles that interact only through the weak force. Although neutrinos are very abundant in the universe, due to their low cross-sections they were not observed until 1953 (Cowan et al. (1956)). This experiment won a share of the Nobel prize for F.Reines in 1995.

The neutrino was first postulated much earlier than this by Wolfgang Pauli in 1930. Originally suggested the name neutron, Pauli proposed the particle after studying beta decay electrons and their energy spectra (Pauli (1930)). Previous to this only two particles were known, the proton and the electron. It was thought at the time that beta decay was a two body decay, where an electron was emitted carrying away all the kinetic energy. If this were the case the emitted electron energy should be constant. However, observation showed that electrons displayed a spectrum of energies. Pauli wrote in a letter to a conference that "as a desperate remedy" a third particle was needed, making beta decay a three body decay where an additional particle satisfies energy conservation by taking away the energy not observed in the electron. As this new particle can be created and propagates with a very small amount of energy, Pauli postulated the particle should be low mass, electrically neutral and have a spin of $\frac{1}{2}$, the last to ensure angular momentum conservation. Detecting a neutral particle was, at the time, a large hurdle in particle physics but one that was overcome just a few years later.

In 1932 James Chadwick discovered a neutral object which he also labelled a neutron (Chadwick (1932)). Chadwick's particle however was far too heavy to be responsible for the small amounts of energy taken away in beta decay. This neutral particle was in fact first theorised by Rutherford to explain an inconsistency between the mass of an atom and its charge (Rutherford (1920)). It was thought at the time that atoms could contain electrons, and together with some protons in the nucleus they could form electron-proton doublets. These neutral doublets would allow the addition of more mass without increasing charge in a nucleus. This theory could not explain the intrinsic angular momentum of some nuclei.

In another discovery around this period it was found that all particles have an intrinsic property called spin. After being proposed again by Pauli it was later given its name by Ralph Kronig, George Uhlenbeck, and Samuel Goudsmit. They suggested a physical interpretation of the property where particles spin on an axis (Uhlenbeck & Goudsmit (1925), Duck & Sudarshan (1997)). Spin was formalised by Pauli as a type of intrinsic angular momentum (Pauli (1940)) and whilst the idea of particles spinning on some axis has proven unrealistic, the name has survived. The problem with the idea of a neutron being a neutral doublet is illustrated clearly in the spin of the stable isotope nitrogen-14. N-14 has a measured spin of $+1\hbar$. If nitrogen was made of 7 protons and 7 neutral doublets we would have in total 14 protons and 7 electrons. Both protons and electrons however were known to have spin $\frac{1}{2}\hbar$. There is therefore no way to make an overall spin of one with an even number of nucleons. It was soon realised that the neutral doublet must be a single particle similar to a proton but neutral in charge.

The next stage in the story of Pauli's lighter neutral particle was its inclusion in Erico Fermi's 'Trends to a Theory of beta Radiation' in late 1933 (Fermi (1934)). It was seen after this theory was written as a definite requirement of radioactive models. The challenge to detect what had now been re-dubbed by Fermi the 'neutrino', meaning 'the little neutral one' was great. This was not met until, as previously stated, Fred Reines and Clyde Cowan Jr succeeded in observing neutrinos some 23 years later.

The significant challenge in detecting the neutrino comes from its properties. The neutrino is neutral and therefore does not leave an ionisation path that can be detected like an electron or proton. To detect the particle's presence, observation of particles made from a neutrino interaction must be made, and as it interacts only through the weak force, it has a very small cross-section and therefore a very small chance of interaction. To maximise the chances of seeing a neutrino Reines and Cowan knew that they would need the biggest source of neutrinos they could find and the largest amount of detecting material they could afford.

The largest source of neutrinos they had at the time came from fission reactions, either those in a nuclear bomb or a fission reactor.

Neutrinos are produced in fission reactions through repeated β-decay of fission fragments.

Reines and Cowan's first thought for a source was a nuclear bomb. The initial plans for dropping a bomb near a shielded detector were however deemed less feasible than a longer experiment with a reactor when they learnt that a reactor could produce an anti neutrino flux

of $\sim 10^{13}$ cm^{-2} s^{-1}. The detector used initially was one at Hanford (1953). Results at this site where found inconclusive due to the high background radiation from cosmic rays. In 1955 they designed a new experiment near the Savannah River nuclear reactor where they could place the detector 11 m from the reactor core and 12 m underground. The ground above the detector provided some cosmic shielding and allowed them to produce a more accurate measurement.

The experiment would make use of the reaction,

$$\overline{\nu} + p \rightarrow e^{+} + n \tag{2.1}$$

To identify a neutrino interaction, Cowan and Reines needed to recognise a positron and a neutron in their detector. The detector itself consisted of two tanks of a Cadmium Chloride solution sandwiched between, and on both sides, by liquid scintillator and photomultiplier tubes. A total of 200 litres of water and up to 40kg of $CdCl_2$ was used along with 110 5" Photomultiplier tubes.

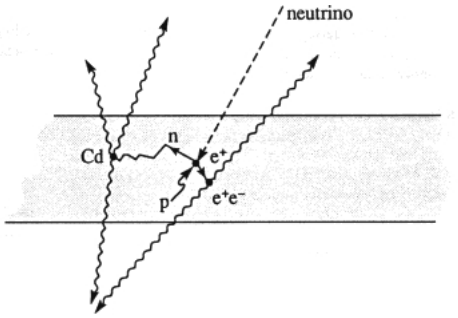

Fig. 2.1. Schematic picture of the neutrino detector at the Savannah River Plant by Reines and Cowan. Image taken from the nobel prize web page (Nobelprize.org (2013)). The interaction shown here illustrates the positron and neutron paths from the neutrino vertex. Explanation of this event can be found in the text.

It is perhaps worth noting here that in comparison to many of the previous experiments listed in this thesis, this was of a much larger scale and perhaps heralded the future of particle physics and the very large detectors now in use.

The positron, an anti-electron, will quickly slow down in the water and annihilate with an electron. This reaction will create two 0.5 MeV gamma rays in opposite directions that should show as a signal in the scintillator layers. The neutron will again be slowed by the water and a few micro seconds later should be captured by the Cadmium nucleus. The Cadmium nucleus becomes an excited isotope and soon emits a number of gamma rays that should be seen in the

surrounding scintillator. By looking for a coincidence between these two signals, background events could be removed and a neutrino signal should be highlighted. The experiment was repeated with both the reactor on and off. When analysed, Cowan and Reines showed there was a net gain in events when close to the reactor and so proved the existence of the anti neutrino $\overline{\nu}$.

Since this discovery, interactions due to neutrino ν_e have been observed also. The suffix is used e here to identify this neutrino as one that seems to be partnered in some way to the electron. Over the years since the discovery of ν_e, observations have been made of two more 'flavours' of neutrino. These new types are very similar to ν_e, but are paired not with electrons, but with newly discovered electron-like particles called muons and taus. The ν_μ was discovered in 1962 by Leon Lederman, Melvin Schwartz and Jack Steinberger (Danby et al. (1962)). Finally, the last to be discovered was the ν_τ in 2000 by the DONUT experiment at Fermilab (Hoshino (2000)).

Strong evidence in favour of there being no additional light neutrinos comes from studies of the invisible Z boson partial decay width. The number of light neutrino types has been found to quite high accuracy.

$$\text{Number of light neutrinos types} = 2.9840 \pm 0.0082 \text{ (Beringer et al. (2012))}$$

where light neutrinos are defined in this case to be less than half the mass of a Z boson, and where the Z boson mass is listed as

$$91.1876 \pm 0.0012 \text{ GeV (Beringer et al. (2012))}$$

The model constructed to help try and explain the existence of neutrinos and all fundamental particles observed in particle physics is our next topic.

2.2 Standard Model

The Standard Model of particle physics is a very successful theory built to explain interactions through three 'fundamental' forces, the electromagnetic, and the weak and strong nuclear. It was constructed by a number of scientists and grew from the theories that combined the electromagnetic force and weak nuclear force together. The construction of electro-weak

theory started in the 1960s with work by Sheldon L. Glashow (Glashow et al. (1970)). A Nobel prize was given in 1979 for this work to Glashow, Abludus Salam and Steven Weinberg (Nobelprize.org (2012)).

The electromagnetic force involves interactions between charged particles. The mediator of electromagnetic interactions is the photon which is a massless particle with a spin of +1. The photon and all particles with integer spin are given the name bosons. Weak interactions exist between particles with half integer spin. The name given to these particles are fermions, with their interactions mediated through the W and Z bosons rather than the photon. The third fundamental interaction included in the Standard Model is the strong nuclear force. The strong force acts on particles that have the property 'colour'. Particles with colour are called quarks with the strong force mediated through the gluon boson. Figure 2.2 nicely illustrates the particles discussed here. In addition, each fermion has an antiparticle. Each antiparticle has similar properties to its fermion counterpart but with an electric charge, of opposite polarity.

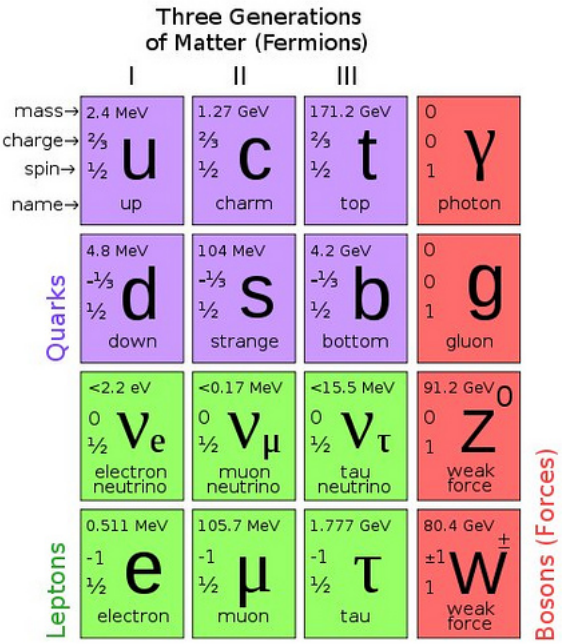

Fig. 2.2. The diagram shows the discovered particles described in the Standard Model. (Wikipedia (2011)).

Neutrinos are neutral in charge and colour so only interact with other fermions via the weak force.

2.3 Weak Interactions

Weak interactions are propagated by three bosons, the Z^0, W^+ and W^-, and can be divided into two types: Charged Current interactions where charge exchange over the interaction is possible are propagated by the two W bosons, and Neutral Current interactions which is mediated by the Z boson and only momentum and energy are exchanged and charge remains constant.

2.3.1 Charged Current

Charged Current (CC) interactions allow us to label a neutrino with a flavour. Through the emission or absorption of a $W^{\pm}$ boson, a neutrino can convert to its charged lepton partner of the same flavour. This conversion is the only way a flavour label can be given to a neutrino. There are three main types of CC interaction observed.

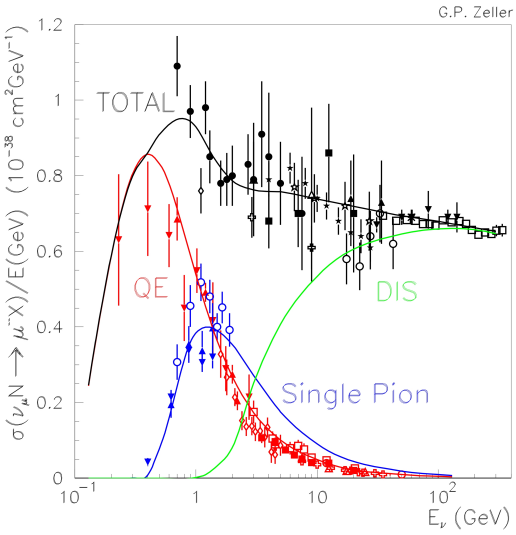

Fig. 2.3. The figure shows CC neutrino cross sections divided by energy as a function of neutrino energy. This plot is included here to identify the leading neutrino interaction channel across an energy scale including that of the T2K experiment. Includes is Quasi-Elastic (QE), resonant single pion, and Deep Inelastic Scattering (DIS) data. The plot makes use of data from experimental as well as simulated sources. This plot and information on its construction and discussion of low energy neutrino cross-sections can be found in Zeller (2008).

Each of these are favoured at different energies as shown in figure 2.3 (Zeller (2008)).

The T2K neutrino beam is made up of predominantly ν_μ and peaks at an energy of 700 MeV. At this energy and up to 1.1 GeV the Charged Current Quasi-Elastic (CCQE) interaction is dominant (figure 2.3). In this interaction a neutrino will interact with a neutron and convert to

a charged lepton and recoil proton. This then makes a two body final state interaction. Both the proton and charged lepton can be easily identified. The lepton will take the majority of energy from this interaction, and so through analysis of its path an observation of the incident energy can be made. This CCQE channel is in fact the primary method used to observe the incident neutrino beam energy in the T2K near detector (ND280).

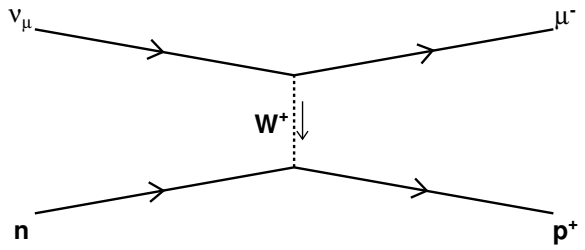

Fig. 2.4. The Feynman diagram of the Charged Current Quasi-Elastic interaction between an incident ν_μ and a target nucleus. This interaction sees the exchange of a virtual W^+ between the ν_μ and a down quark in a neutron inside a nucleus. The ν_μ changes to a charged μ^- that will then travel from the interaction with a large proportion of the incident ν_μ momentum. The down quark then changes to an up quark, converting the neutron into a proton.

As we climb the energy spectrum of the T2K beam, Charged Current Non Quasi-Elastic events (CCnQE) start to become an increasing background to the CCQE signal. CCnQE events are charged-current events in which the final state contains more than simply the scattered nucleon and charged lepton. At T2K energies, the dominant contribution to the CCnQE cross-section is production and decay of the $\Delta(1232)$ (Hernandez et al. (2010)). This resonant Δ then quickly decays to a neutral pion and a proton (figure 2.5). This interaction will be a main focus of the later parts of this thesis with one variant, the emission of a neutral pion in the ND280 Detector, of particular interest. The challenge in detecting this interaction is identifying and understanding the pion in the final state.

The CC1π^0 interaction offers a specific challenge in reconstruction. The planned use of this channel was to test and understand reconstruction processes, provide information for a study into the very important Super-Kamiokande background from the neutral current π^0 production and finally to offer some understanding of the higher energy ν_μ produced in the beam. The π^0 has a mean life of $(8.4 \pm 0.4) \times 10^{-17}$s (Beringer et al. (2012)) and will quickly decay into the products seen in Table 2.1.

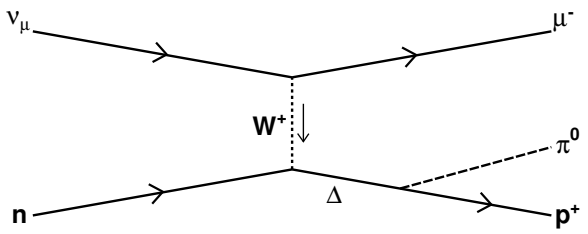

Fig. 2.5. The Feynman diagram of the Charged Current single neutral pion interaction between an incident ν_μ and a target nucleus. The interaction is an example of a CCnQE interaction. This interaction sees the exchange of a virtual W between the ν_μ and a down quark in a neutron inside a nucleus. The ν_μ changes to a charged μ^- that will then travel from the interaction with a large proportion of the incident ν_μ momentum. The down quark changes to a up quark, converting the neutron into a Δ^+. This resonant Δ quickly decays to a proton and neutral pion.

π^0 Decay Modes	Fraction (Γ_i / Γ)	Scale factor
2γ	(98.823 $\pm$ 0.034)%	S=1.5
$e^+e^-\gamma$	(1.174$\pm$ 0.035) %	S=1.5

Table 2.1. Included here are only the two common π^0 decay modes, the third having a branching fraction on the order of 10^{-5}. In this thesis the most common $\pi \to 2\gamma$ will be the focus due to the low numbers of ν_μ interactions seen.

The decay photons form the π^0 will propagate through the ND280 along with the charged lepton from the neutrino interaction. Two photons plus a charged lepton, usually a muon due to the high number of muon neutrinos produced in the beam, becomes the primary signal which must be investigated when analysing this CC1π^0 channel. An additional challenge may come from the lower energy photons converting to a positron-electron pair in nearby material creating additional charged lepton tracks. As noted in Table 2.1 there is a chance of $\pi^0 \to e^+e^-\gamma$ decay. This decay shows the production of a positron and electron in the interaction itself and as stated above increases the complexity in the detection of this channel.

As we again move up the energy scale to 10 GeV, neutrino interactions start to favour Deep Inelastic Scattering (DIS). In this interaction the higher energy neutrino will interact with the quarks making up the nucleons of the target nucleus. Due to the larger energy of the incident neutrino the interaction can now "liberate" the quarks from the targeted nucleus creating hadronic showers. These will be rare during the T2K experiment due to the high neutrino energy required.

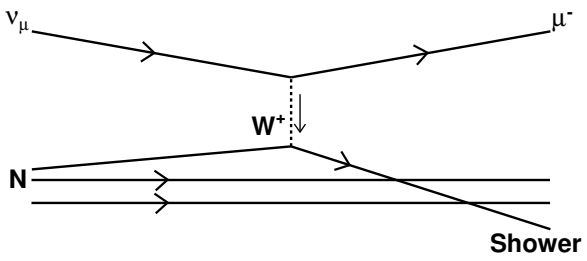

Fig. 2.6. An example Feynman diagram of a Deep Inelastic Scattering (DIS) interaction. Through the exchange of a W boson an incident ν_μ scatterers off a target nucleus. Due to the high incident neutrino momentum, this scattering will impart enough energy to the target nucleons' quark structure to liberate a quark creating hadronic showers.

2.3.2 Neutral Current

The Neutral Current interaction is mediated by the Z^0 boson. This neutral propagator means that charge exchange is not possible with this type of interaction. Neutral current interactions at lower energies will not change the target nucleus. The neutrino will scatter and leave no possible observation for T2K. At higher energies however the energy exchange as the neutrino scatters can alter the target nucleons. This interaction is one of large importance for the T2K experiment as it is responsible for a challenging background in the detection and measurement of ν_e. The higher energy will allow the production of pions through a Δ resonance, similarly to pion production observed through CCnQE interactions.

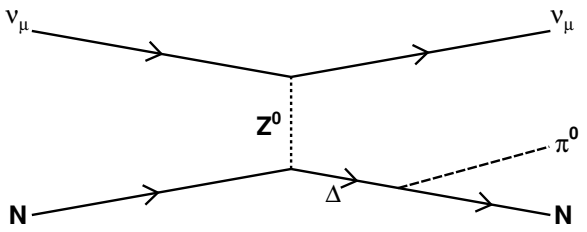

Fig. 2.7. This Feynman diagram shows a neutral current interaction between a target nucleonic neutron and a ν_μ.

This interaction may create a π^0 which will quickly decay into two photons (see table 2.1). The electromagnetic showers in calorimeters and rings produced in water Cherenkov detectors by the photons are very similar to those produced by electrons in the CC ν_e interaction. This being a target signal in the T2K experiment and the search for $\nu_\mu \rightarrow \nu_e$ oscillations. Understanding π^0 production and the cross-section of this interation is therefore of vital importance.

2.4 Neutrino Oscillations

The history and discovery of neutrino oscillations is a very interesting topic which has been discussed many times in a variety of media. For an excellent early discussion of discoveries and the solar neutrino problem see Bahcall and Davis' 1976 paper (Bahcall & Davis (1976)). Due to the wide variety of papers on the subject, and in the interest in moving forward to the theory of Neutrino Oscillations, the history of this topic will not be included in this thesis.

A citation to B. Kayser here feels appropriate as it is through his lectures and papers that the author has an understanding of neutrino oscillations and as such any proof given here will follow Kayser's explanation (Kayser (2004)). In addition throughout this discussion natural units will be used with $\hbar$ = c = 1.

Neutrino oscillations can be defined simply as a non-conservation of neutrino flavour when propagated. So far in this thesis, neutrinos have been defined only by their flavour states, $\nu_\alpha(\alpha = e, \mu, \tau)$. This discussion will show that if neutrinos oscillate they must have mass and therefore mass eigenstates. A mass eigenstate is a state with a defined mass. This mass is conserved and, as such, a mass eigenstate will remain the same state if left in a vacuum. As an example, charged lepton flavour states are the same as their mass eigenstate. A propagating muon will, excluding interactions, remain a muon.

It is therefore possibly more instructive to think of neutrinos not in the flavour states but as a set of three mass eigenstates $\nu_i(i = 1, 2, 3....)$, each of which is a combination of flavour states:

$$|\nu_i >= \sum_\alpha U_{\alpha i} |\nu_\alpha > \tag{2.2}$$

where $U_{\alpha i}$ is the αi^{th} component of a unitary matrix, called the Pontecorvo-Maki-Nakagawa-Sakata (PMNS) matrix. This neutrino mixing matrix describes the mixing of the flavour eigenstates to the mass eigenstates.

Experimentally, oscillations are observed from a disparity the charged lepton flavours produced after some propagation distance. Figure 2.8 illustrates how a neutrino flavour oscillation is observed.

Calculating the probability of an oscillation will allow the prediction of a probability of flavour change and enable the mixing parameters to be understood.

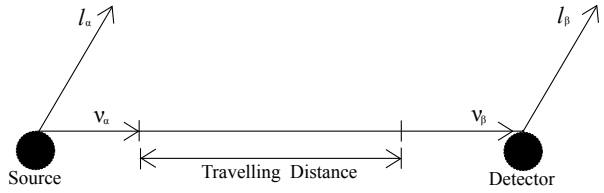

Fig. 2.8. An illustration of an oscillation. Shown here is a neutrino produced at some source labelled by a charged lepton partner to be flavour α. After propagating over some distance it is detected and labelled by a charged lepton as flavour β. Adapted from Kayser (2004).

In the remainder of this section, the mathematical formalism of neutrino oscillations in vacuum will be developed, following Kayser (2004). Using this formalism, the results from T2K and other neutrino oscillation experiments can be interpreted to constrain the elements of the PMNS matrix U and the mass splitting of the neutrino mass eigenstates ν_i.

It should be noted that propagation of neutrinos through dense matter can enhance flavour change, a phenomenon known as the MSW effect (Mikheev & Smirnov (1986), Wolfenstein (1978)). This is caused by charged-current interactions between ν_e (but not ν_μ or ν_τ) and the electrons present in the material. For T2K, with its relatively short baseline, the MSW effect is negligible and hence will not be considered further in this thesis (details found in Kayser (2004)).

2.4.1 Neutrino Oscillations in Vacuum

To calculate the amplitude we'll make use of mass eigenstates. Oscillations in terms of mass eigenstates will look a little different from the picture shown in figure (2.8). With an amplitude $U^*_{\alpha i}$ the W boson decays, creating the neutrino ν_i and the charged anti-lepton $\bar{l_\alpha}$. The same ν_i then propagates over some distance to a detector where it has an amplitude $U_{\beta i}$ to produce charged lepton $\bar{l_\beta}$.

The quantum mechanical amplitude for a neutrino oscillation has three components: an amplitude describing the creation of our neutrino $U^*_{\alpha i}$, a propagation term $Prop(\nu_i)$ and finally the amplitude factor to describe how the neutrino at a later time acts on interaction, $U_{\beta i}$.

This put together will make:

$$\mathrm{Amp}(\nu_\alpha \to \nu_\beta) = \sum_i U^*_{\alpha i} \mathrm{Prop}(\nu_i) U_{\beta i} \tag{2.3}$$

To describe the propagating neutrino a solution to the Schrödinger equation in the neutrinos rest frame is needed

$$i\frac{\partial}{\partial\tau}|\nu_i(\tau_i)>=m_i|\nu_i(\tau_i)> \tag{2.4}$$

where τ_i and m_i are the time and mass in the neutrino rest frame. The solution to this is:

$$|\nu_i(\tau_i)>=e^{-im_i\tau_i}|\nu_i(0)> \tag{2.5}$$

After propagating for time τ_i the amplitude will be

$$<\nu_i(0)|\nu_i(\tau_i)>=e^{-im_i\tau_i} \tag{2.6}$$

This expression then describes the amplitude that one element of the mass eigenstate mixture will propagate for a time in its rest frame equal to τ. It is useful to re-express equation 2.7 in more easily measured terms. This can be achieved by describing $m_i\tau_i$ in terms of lab variables.

Through relativistic invariance this can describe $m_i\tau_i$ by

$$m_i\tau_i = E_it - p_iL \tag{2.7}$$

where t and L are the time and distance from source to detector in the lab frame.

To progress further I will use the fact that for a coherent interfering beam of mass eigenstates, every eigenstate must have the same energy. A thorough proof of this is available from Stodolsky (1998). To help with understanding at this point, however, a simple basic proof will be given.

I will consider only two components of the neutrino beam for simplicity; both will have individually different energies E_1, and E_2. These two components will pick up a phase factor after a time t given by

$$e^{-iE_jt} \tag{2.8}$$

where j = 1, 2.

This phase difference will cause interference in the beam between the components, equal to the difference between the two phase factors. If this interference term is averaged over time t it will vanish unless the two energies are equal. That is

$$< e^{-i(E_1-E_2)t} >_t = 0 \tag{2.9}$$

unless $E_1 = E_2$.

Therefore for the beam to oscillate, the individual mass eigenstate components must each have the same energy E. This provides us with a further way to simplify equation 2.8, and therefore the amplitude of oscillation. Together with the knowledge that the energy of the neutrino will be much larger than the neutrino mass, I will expand each component's individual momentum term p_i:

$$p_i = \sqrt{E^2 - m_i^2} \approx E - \frac{m_i^2}{2E} \tag{2.10}$$

Equation 2.8 now becomes:

$$m_i \tau_i \approx E(t-L) - \frac{L m_i^2}{2E} \tag{2.11}$$

The first term in this equation is constant over all components, and so when averaged over time, this term will vanish as an overall phase for all components. This then, provides us with all the ingredients needed to complete the oscillation amplitude, and find a final expression for the amplitude of an oscillation between neutrino flavour α and β:

$$\text{Amp}(\nu_\alpha \to \nu_\beta) = \sum_i U^*_{\alpha i} e^{\frac{-m_i^2 L}{2E}} U_{\beta i} \tag{2.12}$$

If we take the squared magnitude of this term we will find the probability of a neutrino oscillating between two flavours over a length L, and with energy E.

$$\sum_i U^*_{\alpha i} e^{\frac{-im_i^2 L}{2E}} U_{\beta i} \cdot \sum_j U^*_{\alpha j} e^{\frac{im_j^2 L}{2E}} U^*_{\beta j} \tag{2.13}$$

Here we add a zero term. This will give us a term which will have more apparent features. The added term will be:

$$0 = \delta_{\alpha\beta} - (\sum_i U^*_{\alpha i} U_{\beta i})(\sum_j U_{\alpha j} U^*_{\beta j}) \tag{2.14}$$

Here both the bracketed terms shown equal $\delta_{\alpha\beta}$ because these terms refer to a dot product between the α and β rows, which will of course be equal to zero as α and β are orthogonal neutrino states. This therefore means in equation 2.15 we have 0 if α is not equal to β and, $1-1^2=0$, if α equals β.

Adding this term to equation 2.13 and collecting up terms leaves equation 2.16 below,

$$\delta_{\alpha\beta} - \sum_i \sum_j (U^*_{\alpha i} U_{\beta i} U_{\alpha j} U^*_{\beta j}) \left(1 - \exp \frac{-i(m_i^2 - m_j^2)L}{2E}\right) \tag{2.15}$$

This transforms using Demoivre's theorem

$$\delta_{\alpha\beta} - \sum_i \sum_j (U^*_{\alpha i} U_{\beta i} U_{\alpha j} U^*_{\beta j}) \left(1 - \cos\left(\frac{\Delta m_{ij}^2 L}{2E}\right) + i \sin\left(\frac{\Delta m_{ij}^2 L}{2E}\right)\right) \tag{2.16}$$

Using,

$$1 - \cos(x) = 2\sin^2 \frac{x}{2} \tag{2.17}$$

the probability of oscillation becomes

$$\delta_{\alpha\beta} - \sum_i \sum_j (U^*_{\alpha i} U_{\beta i} U_{\alpha j} U^*_{\beta j}) \left(2\sin^2\left(\frac{\Delta m_{ij}^2 L}{4E}\right) + i \sin(\frac{\Delta m_{ij}^2 L}{2E}\right) \tag{2.18}$$

the summed product of matrix elements has terms that can be cancelled. In addition, by noting the the expression being summed is symmetrical under exchange of i and j, the sum over all values of i and j except $i = j$ is equal to twice the sum over $i > j$.

$$P(\nu_\alpha \to \nu_\beta) = \delta_{\alpha\beta} - 4\sum_{i>j} \Re(U^*_{\alpha i} U_{\beta i} U_{\alpha j} U^*_{\beta j}) \left(\sin^2 \left(\frac{\Delta m^2_{ij} L}{4E} \right) \right) + 2\sum_{i>j} \Im(U^*_{\alpha i} U_{\beta i} U_{\alpha j} U^*_{\beta j}) \left(\sin \left(\frac{\Delta m^2_{ij} L}{4E} \right) \right) \tag{2.19}$$

This expression shows clearly the requirement of neutrino masses, if oscillations are observed. This can be shown here due to the presence of the Δm^2_{ij} terms. With a requirement of a difference in masses between eigenstates, all neutrino masses cannot be zero.

2.4.2 A Massive Neutrino in the Standard Model

The neutrinos were originally placed in the Standard Model in a $\mathrm{SU}(2)_L$ group with neutrinos coupled with charged leptons as a lepton doublet, this coupling mirroring that of quarks, creating the fermionic fields,

$$\begin{pmatrix} \nu_i \\ l \end{pmatrix}_L, l^i_R, \begin{pmatrix} u \\ d \end{pmatrix}_L, u^i_R, d^i_R \tag{2.20}$$

Here ν labels neutrinos, l labels charged leptons, and u and d label up and down type quarks. In this formulation, each field is labelled R and L; meaning right and left chiral fields respectively. It should be noticed that neutrinos do not have a right handed term. This was originally not included, as a right handed fermion required giving a particle mass through a Dirac mass term. As originally neutrinos were thought to be massless, a term was not included. Before continuing to the implications of adding a right handed neutrino, let's first briefly review chirality and mass terms for clarity.

The chirality (handedness) can be thought of similarly to the property helicity which describes the relationship between a particle's direction of motion, and the particle's spin axis. If a particle's momentum is parallel to its spin axis, the particle is right handed; if they are anti-parallel the particle is left handed. Chirality (handedness) for massless particles is the same as its helicity. With massive particles however, they differ as helicity is not Lorenz invariant. This is because a massive particle can be observed with the same spin direction but travelling in the opposite direction if an observation is made from a frame moving at a higher velocity along the direction of the particle's momentum. This marks the difference between helicity and chirality. Chirality is invariant under Lorenz transformation and helicity is not. This makes chirality or handedness a constant property of a particle or field.

A particle field can always be separated into its right and left handed components, so that

$$\Psi = \Psi_R + \Psi_L \tag{2.21}$$

Left and right handed fermions were found to behave differently under weak interactions, i.e. chiral symmetry is not conserved. The right handed fermions have zero weak isospin, and so take no part in weak interactions as they do not couple with the W or Z bosons.

A Dirac mass term is how mass is added to other fermions in the SM and is an interaction between right and left handed particle fields. Adding a Dirac mass term to the SM Lagrangian it will take the form

$$-m_D(\bar{\nu}_L \nu_R + \bar{\nu}_R \nu_L) \tag{2.22}$$

The addition of a right handed neutrino can however give rise to other terms in the Lagrangian. A Majorana term that can also add mass to the neutrino:

$$-m_M^L(\bar{\nu}_L^c \nu_L + \bar{\nu}_L \nu_L^c) - m_M^R(\bar{\nu}_R^c \nu_R + \bar{\nu}_R \nu_R^c) \tag{2.23}$$

This term turns a neutrino to an anti-neutrino or an anti-neutrino to a neutrino meaning that neutrinos can no longer be distinguished from their anti-particle. This process is allowed by all conservation laws of the SM. It should be noted however that is does break the accidental symmetry of lepton number. Whether a neutrino is a Majorana particle or a Dirac is still to be answered. Investigation into processes such as neutrinoless double beta decay that can only occur with Majorana neutrinos are still ongoing (Barabash (2011)).

2.4.3 PMNS Matrix

In equation 2.2 a neutrino mass eigenstate is expressed as a combination of the 3 flavour eigenstates. The PMNS (Pontecorvo-Maki-Nakagawa-Sakata) Matrix is a 3 x 3 unitary matrix which describes neutrino mixing.

$$\begin{pmatrix} \nu_e \\ \nu_\mu \\ \nu_\tau \end{pmatrix} = \begin{pmatrix} U_{e1} & U_{e2} & U_{e3} \\ U_{\mu 1} & U_{\mu 2} & U_{\mu 3} \\ U_{\tau 1} & U_{\tau 2} & U_{\tau 3} \end{pmatrix} \begin{pmatrix} \nu_1 \\ \nu_2 \\ \nu_3 \end{pmatrix} \tag{2.24}$$

This can be written as a product of three rotation matrices with one having a phase δ. The phase will cause Charge Parity (CP) violation in neutrino mixing if it sits with a non-zero contributing term.

$$U = \begin{pmatrix} c_{13}c_{12} & c_{13}s_{12} & s_{13}e^{-i\delta} \\ -s_{12}c_{23} - c_{12}s_{23}s_{13}e^{i\delta} & c_{23}s_{12} - s_{13}c_{12}s_{23}e^{i\delta} & s_{23}c_{13} \\ s_{12}s_{23} - c_{12}s_{23}s_{13}e^{i\delta} & -c_{23}s_{12} - s_{13}c_{12}s_{23}e^{i\delta} & c_{23}c_{13} \end{pmatrix} \begin{pmatrix} e^{i\alpha_1/2} & 0 & 0 \\ 0 & e^{i\alpha_2/2} & 0 \\ 0 & 0 & 1 \end{pmatrix} \tag{2.25}$$

c_{ij} here translates to $\cos\theta_{ij}$, similarly $s_{ij} = \sin\theta_{ij}$.

The phases α_1 and α_2 are Majorana phases. If neutrinos are Majorana particles these phases will influence neutrinoless double beta decay. The remaining parameters here, θ_{13}, θ_{23}, θ_{12} and the phase δ, combine with the mass differences shown in equation (2.19) to create the list of parameters that govern the oscillations currently observed.

2.5 Neutrino Oscillations to date

In this final section of the chapter, the current best limits on the seven oscillation parameters will be reviewed and discussed. There are two main types of neutrino oscillation experiment: one looking into oscillated neutrinos travelling from the sun to the earth, and the second looking at oscillated neutrinos created and detected in our atmosphere. Atmospheric neutrino oscillation experiments are sensitive to θ_{23} and Δm^2_{23} and so these are often referred to as θ_{atm} and Δm^2_{atm}. Solar neutrino observatories are more sensitive to θ_{12} and Δm^2_{12} dubbed θ_{sol} and Δm^2_{sol}. This sensitivity favouring comes from two factors. The scale of the corresponding mass differences mean that as Δm^2_{12} is significantly smaller than Δm^2_{23}, the distance needed to increase the probability of oscillation is larger. The second comes from a limitation of using the sun, as it produces predominantly ν_2.

First looking at the solar sector results, the best limits for both θ_{12} and Δm^2_{12} come from a three-flavour oscillation analysis of data from both the KamLAND reactor experiment and solar neutrino experiments (Gando et al. (2011)). The solar neutrino data is obtained from chlorine and gallium experiments (Cleveland et al. (1998); Abdurashitov et al. (2009)), Borexino (Arpesella et al. (2008)), SNO III (Aharmim et al. (2008)), the zenith spectra in Super-Kamiokande phase I (Hosaka et al. (2006)), and the day-night spectra in SNO phase I and II (Aharmim et al. (2010)).

The resulting allowed regions in the $(\tan^2\theta_{12}, \Delta m^2_{21})$ plane are shown in figure 2.9 and the best fit values are,

$$\Delta m^2_{21} = 7.50^{+0.19}_{-0.20} \times 10^{-5}\text{eV}^2 \tag{2.26}$$

$$\tan^2\theta_{12} = 0.452^{+0.035}_{-0.033} \tag{2.27}$$

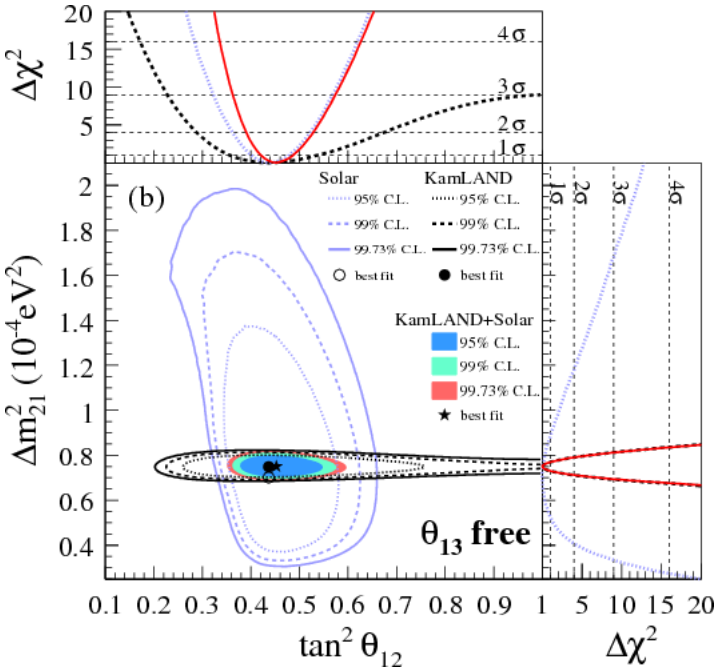

Fig. 2.9. The allowed regions in the $(\tan^2\theta_{12}, \Delta m^2_{21})$ plane for three-flavour analyses of solar and KamLAND data with θ_{13} as a free parameter. The shaded regions are the result of the combined analysis of both data sets. The top and side panel show the projected $\Delta\chi^2$ profiles (Gando et al. (2011)).

The atmospheric sector results come from study of ν_μ disappearance. MINOS uses its long baseline to study the disappearance of ν_μ that are initially produced from an accelerated beam of protons before travelling 735km to the far detector. From data collected from both its near and far detectors, MINOS has the current world leading observation of Δm^2_{23} mass splitting (Adamson et al. (2011)) based on a two flavour approximation with maximal mixing,

$$\Delta m^2_{23} = 2.32^{+0.12}_{-0.08} \times 10^{-3} eV^2 \tag{2.28}$$

(one standard deviation (S.D.) uncertainty)

Whereas the current most accurate measurement of the θ_{23} mixing angle was produced by Super-Kamiokande which studied the oscillation of ν_μ created in the atmosphere (Abe et al. (2011b); Beringer et al. (2012)). This result was obtained using a two neutrino oscillation analysis of data from SK I, II and III,

$$\sin^2(2\theta_{23}) > 0.95 \tag{2.29}$$

(90% C.L.)

However, the MINOS collaboration have recently released preliminary results (Feldman et al. (2013)) which use their complete data set; including additional protons on target, the antineutrino-enhanced beam data, and atmospheric neutrinos and antineutrinos. Though still preliminary, this analysis improves upon the above stated Δm^2_{23} and $\sin^2(2\theta_{23})$ measurements with best fit points of,

$$\Delta m^2_{23} = 2.39^{+0.09}_{-0.10} \times 10^{-3} eV^2 \tag{2.30}$$

$$\sin^2(2\theta_{23}) = 0.96^{+0.04}_{-0.04} \tag{2.31}$$

The previous results can be seen in figure 2.10 and the preliminary updated results, along with published T2K results, can be seen in figure 2.11.

The final mixing parameter to be discussed is θ_{13}. This can be measured directly from $\overline{\nu_e}$ disappearance in reactor experiments and from solar neutrino data and long-baseline accelerator experiments using $\nu_\mu \rightarrow \nu_e$ appearance. However, accelerator experiments are can make a wider range of measurements using different baselines and energies with neutrinos and/or antineutrinos, and are also sensitive to the CP violating phase, the mass hierarchy (through study of matter effects) and θ_{23}.

T2K was the first experiment to report evidence of electron neutrino appearance in June 2011 (Abe et al. (2011a)) and, with many other experiments having released measurements since, θ_{13} has quickly moved from being unknown to becoming a well measured parameter. The Particle Data Group (PDG) have released the best estimate of θ_{13} as being a weighted average of selected experimental measurements (Beringer et al. (2012)) giving,

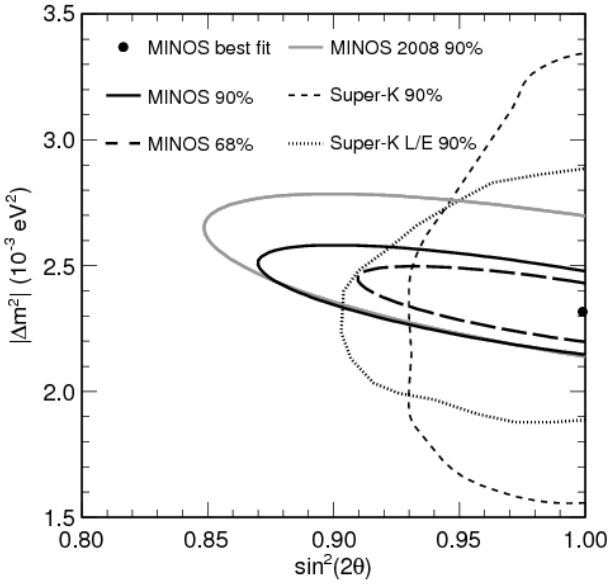

Fig. 2.10. The figure shows likelihood contours around the best fit values for the atmospheric parameters observed by the MINOS accelerator neutrino experiment. Previous measurements from both MINOS and Super-Kamiokande are shown also (Adamson et al. (2011)).

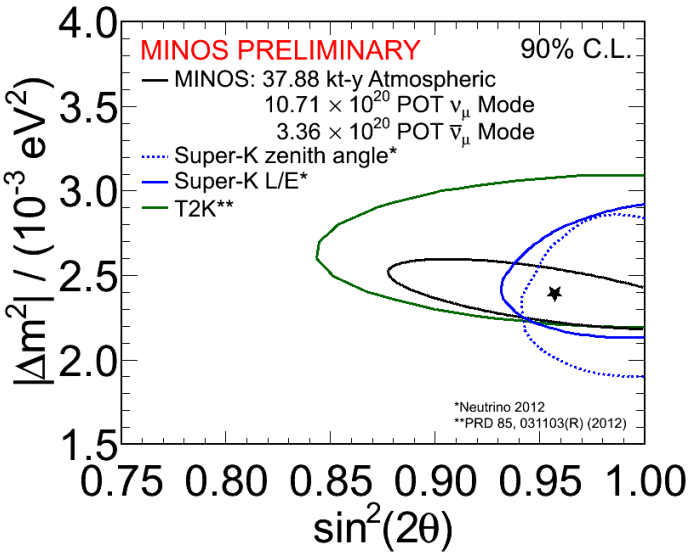

Fig. 2.11. This figure shows 90% confidence limit contours for the preliminary atmospheric parameters obtained by MINOS and published results from T2K and Super-Kamiokande (Feldman et al. (2013)).

$$\sin^2(2\theta_{13}) = 0.098 \pm 0.013 \tag{2.32}$$

A summary of measurements can be seen in figure 2.12.

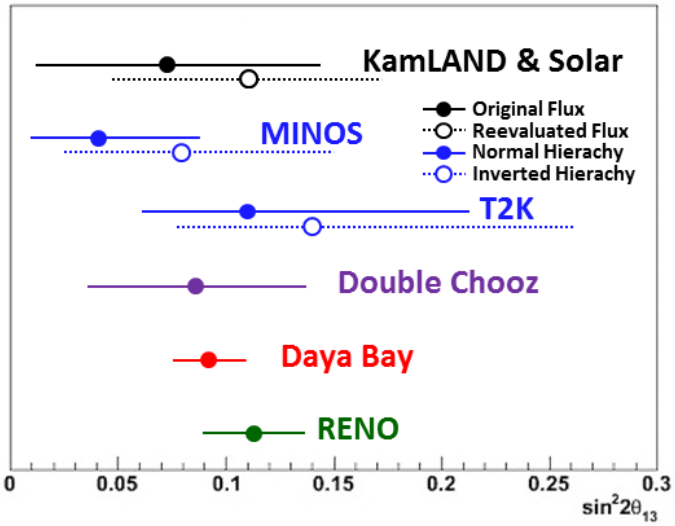

Fig. 2.12. This figure shows a summary of all non-zero measurements of $sin^2(2\theta_{13})$ as of May 2012 (Litchfield (2012)).

This then is the current status in investigations of the neutrino mixing matrix. The remainder of this work will be looking at the T2K experiment which will investigate further the angles θ_{23} and θ_{13} as well as the mass splitting Δm^2_{23}.

Chapter 3

T2K

T2K is a long-baseline neutrino oscillation experiment designed to further investigate muon neutrino mixing. The experiment probes both θ_{13} and θ_{23} mixing angles and will improve precision and understanding of the neutrino mass scale. The design of T2K was specifically optimised for sensitivity to θ_{13}, which had not been measured in particular is of current importance as the last unknown lepton mixing angle.

Specifically, T2K's physics goals are to increase precision of Δm^2_{23} by reducing the uncertainty $\delta(\Delta m^2_{23})$ to approximately 10^{-4}eV^2, to lower $\delta(\sin^2 2\theta_{23}) \sim 0.01$ and to increase the sensitivity of the current best limit on θ_{13} by a factor of 20 more than observations made with the CHOOZ experiment (Apollonio et al. (2003)). The measurement will be made through the study of ν_μ disappearance and $\nu_\mu \rightarrow \nu_e$ oscillations over the distance from beam source to the T2K far detector.

T2K makes use of an off-axis beam (Beavis et al. (1995)) which allows muon neutrino oscillations to be maximised whilst reducing the background of electron neutrinos. An off-axis angle of 2.5° is used, which means that the beam is directed 2.5° away from the far detector.

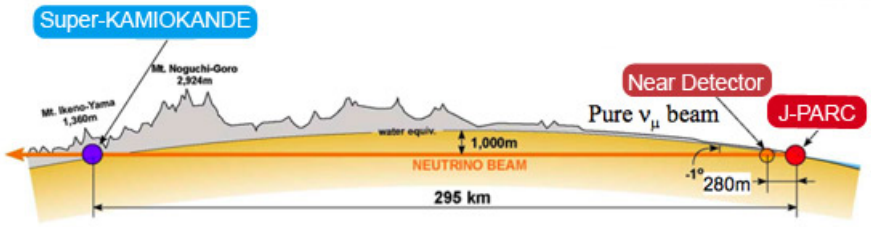

Fig. 3.1. An illustration of the baseline of the T2K experiment from J-PARC to Super Kamiokande. Image taken from T2K (2013).

T2K's experimental hardware is split over two sites. The accelerator, beam source and near detector complex are housed on the east coast of Japan at the JPARC research site. The far detector, Super-Kamiokande (SK) (Fukuda et al. (2003)), is 295 km away on the western side of Japan. SK is a pre-existing detector which has been upgraded for the purpose of the experiment.

However completely new installations were needed at the JPARC site. These included a large upgrade to the beamline, a target station and a full near-detector suit. Two near detectors were commissioned for T2K: the on-axis detector INGRID aims to measure the flux and profile of the T2K beam whereas ND280, the off-axis detector, is a multi-purpose detector which aims to characterise the beam before it travels to SK. Understanding the beam characteristics here is essential to studies of both signal and background events at SK.

3.1 JPARC Accelerator

The JPARC accelerator is situated at Tokai, Ibaraki and contains three accelerators Yamazaki et al. (2003): a linear accelerator (LINAC), a rapid-cycling synchrotron (RCS) and a main ring synchrotron (MR).

Fig. 3.2. The figure shows the layout of the JPARC Research Complex. Labelled on this figure is the design energy of JPARC's 50GeV high intensity proton beam, however during the start of the experiment and during the author's involvement with the project the beam was operating at the commissioning energy of 30GeV. Image taken from IRFU (2013).

A beam of H^- is accelerated by the J-PARC LINAC, this is currently operating at 181 MeV though it is hoped that this will increase to 400 MeV in future. These charged Hydrogen atoms are then stripped of their electrons to form a proton beam; this happens when they pass charge stripping foils at the RCS injection. In the RCS, the beam is accelerated to 3 GeV at a 25 Hz cycle, with two bunches accelerated per cycle. Approximately 5% of the accelerated protons are injected into the MR, the rest sent to other experiments in the JPARC facility. During the authors time with T2K, which was before June 2010, the MR accelerated six bunches per

cycle, although currently this has increased to eight bunches. The MR has two extraction points, one slow and one fast. The slow extraction services a hadron beamline whilst the fast extractor places protons into the T2K neutrino line.

3.2 Neutrino Beamline

The beamline is composed of two sections, as seem in figure 3.3. The first extracts protons which are directed toward Kamioka and the T2K far detector (1). The second (2) section takes protons to a target (4), here the protons are used to create a pion beam. This beam is focused by a series of magnetic horns (3) then given space to decay (5). The decay products are predominantly muons and muon neutrinos produced in a two body decay. The muons pass through a muon monitor (6) before being stopped in nearby rock. The monitor is designed to measure the angle of the beam to better than 0.25 mrad and the stability of beam intensity to better than 3%. The muon neutrinos produced in the decay propagate through the T2K near detectors and onto the far detector. This beam can be tuned to off-axis angles from 2.0° to 2.5°. The beam angle and the distance to the far detector at Kamioka is measured by a GPS survey.

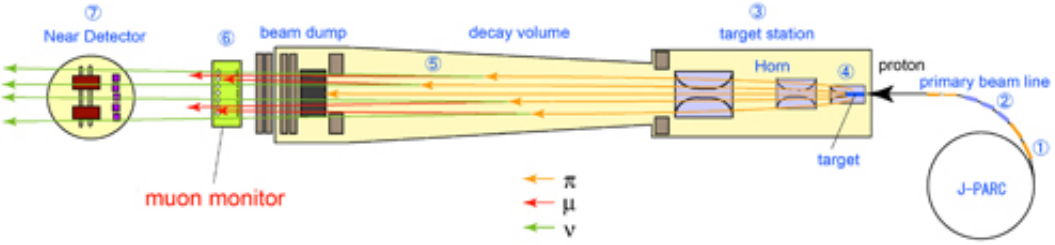

Fig. 3.3. The figure illustrates the T2K beamline. After extraction from the JPARC accelerator the beam is propagated through to a decay volume where pions will decay into muons and muon neutrinos. The muon neutrinos then pass through the T2K near detectors before continuing onto the T2K far detector Super-Kamiokande. Figure taken from T2K (2013).

3.3 ND280 Near-Detector Suite

At the JPARC research complex, the T2K experiment has two near detectors. They are housed in a newly built pit 280 m from the beam target and aim to profile the neutrino beam, as well as perform other useful physics studies before its propagation to the T2K far detector Super-Kamiokande (SK).

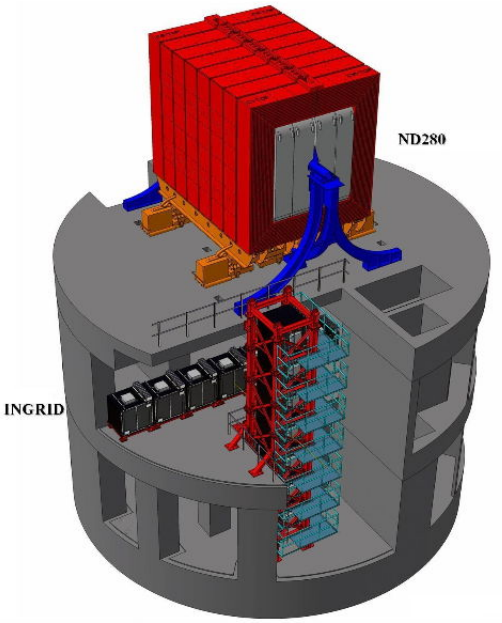

Fig. 3.4. The figure shows a 3D image of T2K's near detector pit, including relative positions of the two detectors. The ND280 sits above Ingrid to order to match the off axis angle of the far detector Super-Kamiokande. The ND280 is designed to profile the off-axis portion of the beam, as well as provide observations of cross-sections which are of particular importance to the experiment. The beam in this image is directed at an angle through the page, passing through the opening in red UA1 magnet used in the ND280 detector.

3.3.1 On Axis Detector (INGRID)

The INGRID detector (Interactive Neutrino GRID) is designed to profile T2K's on axis neutrino beam by monitoring the beam intensity and direction. The detector is constructed from 14 identical modules which cross in the centre with two additional modules to profile the diagonal sections off axis.

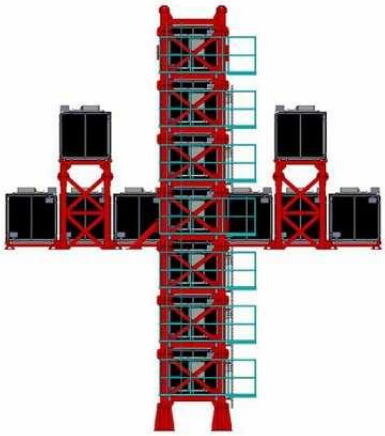

Fig. 3.5. The figure shows an animation of the INGRID near detector. The beam in the image is directed through the page. The image is taken from T2K (2013)

Each INGRID module is constructed of extruded scintillator bar layers sandwiched between iron layers which act as a dense target. Surrounding 11 iron and scintillator layers are veto scintillator layers that will allow the reconstruction and separation of beam events from background. Through comparison of the number of neutrino events reconstructed in each module the beam centre can be measured to a precision better than 10cm. This allows a precision measurement of the angular direction of 0.4 mrad from the beam source 280 metres downstream. This measurement is needed at a high precision to allow an accurate measurement of the off axis angle, on which both the ND280 detector and the far detector are situated.

3.3.2 ND280 Detector: Introduction

The ND280 detector, as shown in Figure 3.4, sits above the INGRID detector. This spacing creates an off-axis angle which mirrors that of the far detector, Super-Kamiokande. This allows the ND280 to profile the same angular region of the neutrino beam which will be propagated to Super-Kamiokande. The detector is designed to fill a number of roles: it must provide observations of the flux, energy spectrum and ν_e contamination in the beam, as well as providing an opportunity to study neutrino interactions. The study of the cross-sections of these interactions will allow improvements to the systematic errors associated with neutrino events at SK.

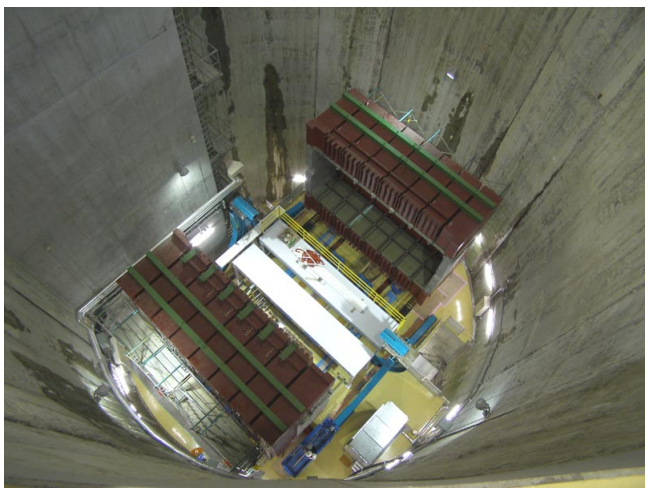

Fig. 3.6. The figure a photograph of the UA1 Magnet in the NDs280 pit. The image was taken before the installation of any of the ND280 inner subdetectors. (Taken May 19, 2009, JPARC Construction Photos)

The ND280 consists of a number of sub-detectors which fit inside the recommissioned UA1 magnet shown in figure 3.6. The magnet produces a dipole field of 0.2T which offers a good momentum resolution calculation, as well as a simple way to determine the sign of charged particles. The gaps in the magnet return yoke are regularly filled in a number of places with detective material which, when used as one large sub-detector, is named the Side Muon Range Detector (SMRD). The SMRD provides a veto for cosmic ray events, a way to label particles originating from interactions in the walls of the detector hall or inside the magnet itself, and finally a way to identify muons that propagate at an oblique angle with respect to the beam direction.

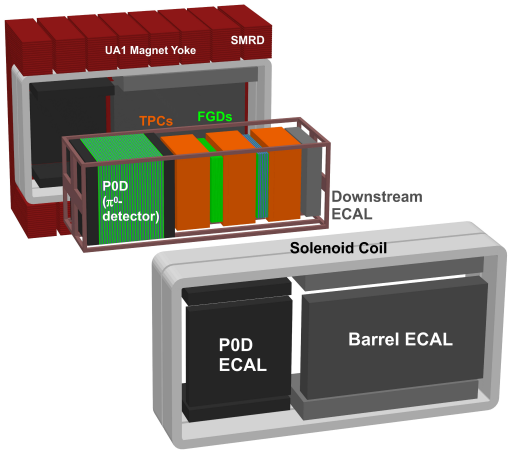

Fig. 3.7. The figure shows an exploded image of the ND280 Detector. The Pi-Zero Detector or P0D is shown here in dark green on the left hand side of the the central basket. Next to the P0D in the basket are the alternating orange TPC layers and green FGD layers. Together the FGD and TPC sub-detectors are referred to as the Tracker Region throughout this thesis. Surrounding both the P0D and the Tracker Region are the ND280's calorimetry, with the Downstream ECAL sitting inside the basket behind the last TPC. The calorimetry differ in design based on their position, these differences will be discussed in more detail later in this thesis. The beam in this image is directed from left to right. Figure taken from T2K (2013)

Figure 3.7 shows that the next layer of detection is electromagnetic calorimetry provided by the 'ECals'. The ECals can be split into two clear sections. The calorimetry surrounding the pi-zero detector is called the P0D-ECal, it is designed to identify any photons that do not convert inside the Pi-zero detector. Surrounding the remainder of the sub-detectors are ECals with finer sampling structure. These are designed to measure photon and charged particle energy deposition and provide directional information for photons created inside the tracker region. These finer structured ECals will be discussed using different names based on their location. The ECals which surround the tracker region on the sides normal to the beam direction are

called the Barrel ECals. The Downstream ECal, or 'DsECal', sits on the beam axis capping the end of the tracker region.

There are two remaining inner regions in the ND280: the P0D and Tracker region. The Pi-zero Detector or 'P0D', designed to study neutrino-induced π^0 events. The tracker region is made up of two different sub-detectors; fine grained detectors and time projection chambers. Two Fine Grained Detectors (FGDs) are sandwiched on beam axis sides by three Time Projection Chambers (TPCs). These, together with the surrounding ECals and SMRD, are designed to achieve all the aims of the ND280, including a second opportunity to study π^0 interactions.

3.3.3 ND280 Detector: Pi Zero Detector (P0D)

The Pi Zero Sub-detector is designed to measure NCπ^0 interactions, specifically, $\nu_\mu + N \rightarrow \nu_\mu + N + \pi^0 + X$ on a water target. This channel is of special interest due to its impact as a background to ν_e events at SK. In order to achieve this goal the Pi-Zero Detector consists of three Super P0Dules. Each Super P0Dule is constructed of pairs of orthogonally oriented layers of triangular scintillator bars interleaved with inert material (brass, water or lead) to serve as a target for neutrino interactions and as absorber for the P0D as a sampling calorimeter. In the case of the Upstream and Central Super P0Dules the inert material is lead, whilst the central Super P0Dules use a brass and water target. This design can be seen in figure 3.8.

Figure 3.8 also clearly illustrates the structure of each active P0Dule. These P0Dules consist of two layers of scintillator containing interlocking triangular scintillator bars. These two layers are laid in orthogonal directions to enable three dimensional tracking and are wrapped together by a thin layer of PVC to prevent light from reaching the bars. Each scintillator bar contains a wavelength shifting optical fibre running through its core. One end of this fibre is connected to a Multi-pixel Photon Counter (MPPC) and the other is mirrored in order to maximise captured light. Each individual P0Dule in the Central Super P0Dule is layered with a sheet of brass upstream from a water target in order to convert photons and enhance the electromagnetic shower production. This water target allows the P0D to make cross section measurements of neutrino-induced π^0 production. An important feature of this design is the P0D's ability to remove the water from its targets. By comparing observations with and without water targets, the P0D clearly isolates the events produced with an oxygen target.

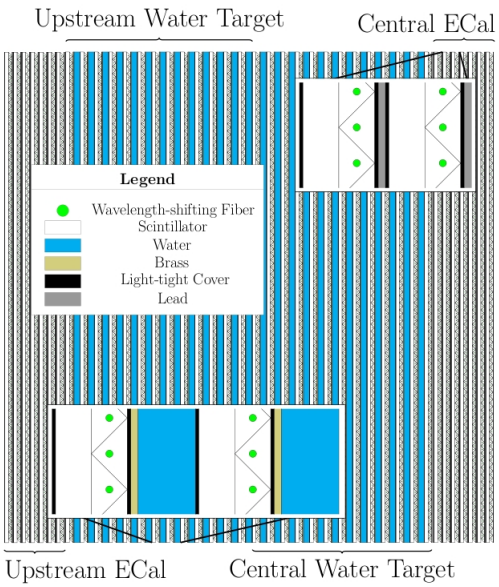

Fig. 3.8. The figure shows a 2D cross section of the P0D sub-detector. The upstream and central ECals are referred to as two of the P0D Super P0Dules, whilst the Upstream and Central Water Targets make up the third. Each Super P0Oule consists of layers of scintillator bars and either brass and water, or lead targets. The beam in this image is left to right. Image taken from Abe et al. (2011c)

3.3.4 Time Projection Chambers

The Time Projection Chambers (TPCs) sit in the tracker region of the ND280 and are designed to achieve a number of goals. The detector produces excellent reconstructions of charged tracks passing through each TPC, and so can be used to identify charged particles. This allows the production of a high purity sample of many different neutrino interactions. Further to this, the detector can also determine the charge of a particle by resolving its curvature in the ND280's magnetic field and provide particle identification through studying the deposition of energy along a trajectory. As seen in figure 3.7 there are 3 TPCs in total surrounding two Fine Grained Detectors (FGD).

Figure 3.9 shows a cut away image of a TPC. Each is split in half by a central cathode, either side of this are two inner drift chambers filled with an argon based drift gas. Between the field cage and the outer wall is an area flooded with CO_2. This acts as both an insulating layer, as well as a barrier to stop oxygen, nitrogen and any other contaminants in the air from contaminating the inner chamber. Charged particles travelling through the drift chamber will produce ionisation electrons in the drift gas. The electrons will then drift to the read-out planes away from the central cathode.

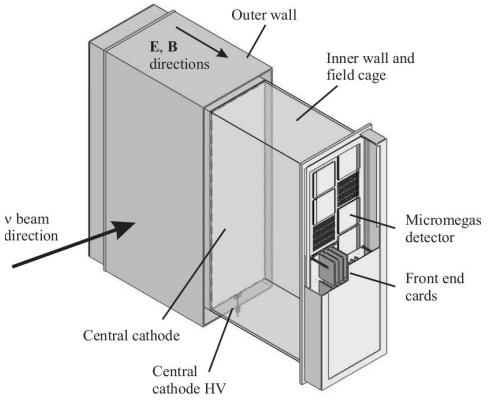

Fig. 3.9. This figure illustrates the structure of the TPC. Figure taken from Abe et al. (2011c)

The TPC uses bulk micromegas detectors for gas amplification. For every read-out plane, there are twelve micromegas modules situated in two offset columns. These modules are constructed by laminating a woven mesh on to a Printed Circuit Board (PCB) covered by a photoimageable film. The micromesh is then sandwiched between two layers of insulating material and undergoes UV exposure followed by chemical development. This bulk manufacturing technique produces mechanically robust detectors with no need for an external frame to hold the mesh, hence minimizing dead areas on the edges of a module and allowing large detection areas with excellent gas gain uniformity. Micromegas devices also show significant advantage over wires in counting rate, simplicity and energy, spatial and time resolution. For further information see Abgrall et al. (2011) and Giomataris et al. (2006).

3.3.5 Fine Grained Detectors

The ND280 has two FGDs which sit between three TPCs. Each FGD provides a target for neutrino interactions in the tracker region and aids in vertex finding and particle tracking. The tracking and vertex identification is achieved from observation of particle trajectories in planes of plastic scintillator. Thin 9.61 mm $\times$ 9.61 mm $\times$ 1864.3 mm scintillators are used to provide fine grained vertex identification, with each bar once again containing a wavelength shifting (WLS) fibre running along a hole at its core. An MPPC read-out is attached to the end of each fibre, whilst the other end is mirrored. The read-out end swaps between adjacent bars allowing better resolution for particles traversing each FGD. The bars are assembled into XY Modules which sit perpendicular to the beam direction. Each XY Module is made of layers of 192 bars, one layer with bars running along the X-axis and the other along the Y-axis. This

alternating pattern enables the FGD to track particles and locate vertices in three dimensions. FGD1 consist of fifteen of these XY Modules whilst the further downstream FGD2 consists of seven XY Modules with 2.5 mm thick polycarbonate water containers.

Similar to its use inside the P0D subdetector, the water target in the FGD2 is used to provide oxygen targets for neutrino interactions. Through comparing observations made in FGD1 and FGD2, the differences in neutrino interactions occurring in water and carbon can be measured. This comparison can then be used to statistically isolate the water only interactions. This statistical separation allows T2K to compare neutrino interactions on water (oxygen) wth those on plastic (carbon), which is important to reduce systematic errors in comparing ND280 data to Super-Kamiokande.

3.3.6 Electromagnetic Calorimeter Design

The calorimetry surrounding the Tracker region is designed to observe and measure particles produced from vertices in the FGDs, and to help provide veto information for cosmic muons. Each ECal is designed primarily to provide a measurement of the energy and direction of particles over an energy range of 500 MeV to 10 GeV, with an expectation that useful measurements could be made of particles with energy as low and 50 to 100 MeV. It is especially important that the Tracker ECals convert and measure the energy and direction of outgoing photons created in the Tracker region. This is because neutral particles will not be observed inside the TPCs.

To convert these relatively high energy particles the ECals must contain a large amount of mass. This large target mass means that neutrino interactions inside the ECals will be frequent. Observations of the interactions will be limited by the coarse nature of the ECals, however the detectors are expected to observe and measure some of these interactions in addition to those with vertices in the FGDs. Identifying simple CCQE muon events will be the primary and initial channel to be studied.

To achieve this remit in the space available, the Tracker ECals were designed and constructed as sampling calorimeters. Each consists of a number of alternating layers of active plastic scintillator and 4 mm thick sheets of lead absorber. Each scintillator layer consists of varying numbers of 4 cm $\times$ 1 cm ended scintillator bars. These bars, similar to the thinner 1 cm $\times$ 1 cm bars used in the FGD and the wider 1 cm $\times$ 5 cm bars used in the INGRID, were constructed at Fermilab. Each scintillator bar is coated with TiO_2 to reflect escaping light back

inside the scintillator in order to increase the photon capture efficiency. The bars making up the layer are orientated so that the layer is 1 cm thick and a multiple of 4 cm wide. The wider bars are used here, as in the INGRID detector, because the detector will be observing particles originating from an interaction vertex in the FGD. Defining the Z-axis to be the direction normal to the lead and scintillator planes, each detector is orientated with this axis pointing towards the inner tracker region. This ensures that all particles leaving the tracker region will pass through the high density lead layers which will aid in the conversion of photons and the showering of electrons and positrons exiting the tracker.

To allow three dimensional tracking of the particles passing through the ECals, each adjacent layer is rotated so that it is perpendicular to the last. Figure 3.10 is included here to help visualise the layer design.

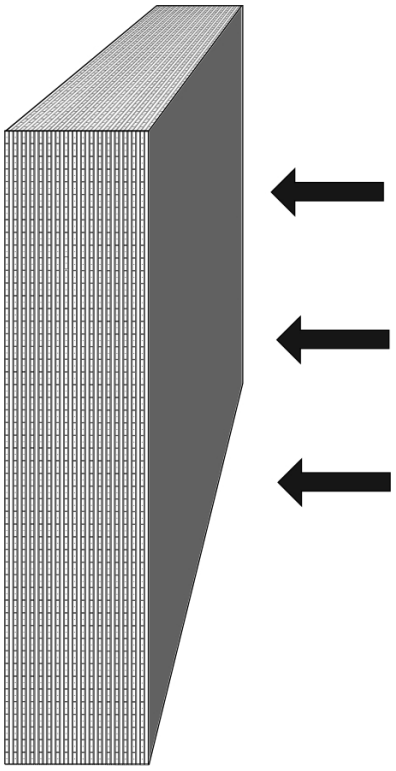

Fig. 3.10. The figure shows a representation of the Downstream ECal's scintillator and lead layers. The arrows included here represent the incoming beam direction. Each layer consists of 50 bars with a sheet of lead above it.

Running along the centre of each bar is a 2 mm hole through which a wavelength shifting fibre is threaded. The end of this fibre is then either mirrored or coupled with a MPPC. Whether an end is mirrored or connected to a MPPC read-out depends on the location in the ND280

detector. The MPPCs themselves are then connected to a Trip-t Front end Board (TFB) via a 1m long mini coaxial cable. The TFB's are then cabled to a Read-out Merger Module (RMM), these boards provide the raw data that is processed by the data acquisition software or DAQ.

Seven Tracker ECals were built in total: two side modules, one downstream module, two top modules and two bottom ECals. The top and bottom modules are split into two in order to allow mounting to the UA1 magnet which opens along the centre to allow access to the inner subdetectors. This design is shown in figure 3.7.

3.3.7 ECal Construction

The first Tracker ECal constructed was the Downstream ECal (DsECal), which also acted as the prototype detector. The construction and much of the production procedure for the detector was developed at Lancaster University in 2007. The author was part of the team that developed the procedures and took a significant role in both the construction and the procedure design and testing.

3.3.7.1 Downstream ECal Layer Construction

For all Tracker ECals, the first stage of construction is layer building. Building a layer refers to the fixing and gluing together of scintillator bars, an aluminium frame and a cover of 1.75 mm thick lead sheeting. During the production of the DsECal, the first stage was re-sizing and painting each piece of 1.75 mm thick 2 m x 1 m lead sheeting. These sheets when paired up would cover the 2 m x 2 m layer of scintillator bars. In testing it was concluded that the adhesion of lead to scintillator was aided by a priming layer of paint and for all other ECal modules this priming stage was done by the suppliers.

Each of the layers was set into an aluminium frame that contained all fixings needed to attach each layer to the next and to the aluminium bulk heads. The frame had a $2cm^2$ cross section and a 2m length. Along two sides of the completed frame were 2mm radius holes which were designed to match with the positions of the holes in the scintillator bars. To keep each layer accurately within size tolerances, the aluminium frame was fixed to a large layer production table.

Araldite glue was used throughout the construction of the layers and, as with the paint application, many gluing methods were investigated. Using a compressed air gun room temperature glue was applied, which was then spread over the sides and top of the bars with a large

spatula, was concluded to be the best. Before laying the bars in place, the frame glue must first be applied to the sides of the bars. To do this the bars were clamped on their sides on a separate bench. Once complete the bars were moved over to their final position inside the aluminium frame. Here they are catalogued and recorded. This record was part of a chain of recorded information for the channel which starts with the manufacture information and the first stage of QA and ends with the final calibration and testing of the completed detector.

The next stage of the layer building procedure was to insert pins through the aluminium frame and into the holes in the scintillator bars. These pins were designed to hold the bar in place and stop the glue from entering the hole. This stage of the layer building procedure under went a large change from the original plan. After construction of the first prototype layer it was found that glue had entered and blocked the holes. The reason for this fault was the shape of the fibre hole along the bars. The hole was designed to be circular with a diameter of 1 mm, but the bars produced had an oval shaped hole with a length as long as 3 mm, this can be seen in Figure 3.11.

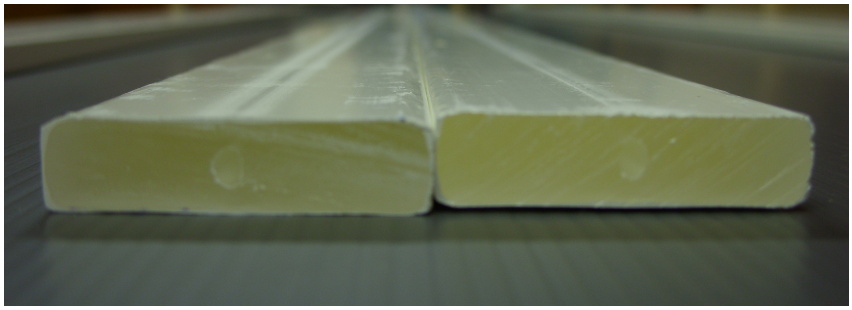

Fig. 3.11. The figure shows the oval rather than circular fibre hole that was produced in the ECal 4 cm x 1 cm cross-section bars. Image taken at Lancaster University by a member of the construction team.

This issue arose due to difficulties when extruding scintillator bars during their manufacture. The bars undergo an extrusion process that involves joining two halves of the scintillator around a peg that should mark out the designed hole. It was found that a circular hole was unachievable with this process and the bar dimensions requested. To overcome this issue a new pin design was developed by A. Grant who is based at Daresbury Laboratory UK. Disposable rubber rings were pushed onto the bar by a newly designed pin allowing a better seal around the elongated hole. This new design is illustrated in figure 3.12.

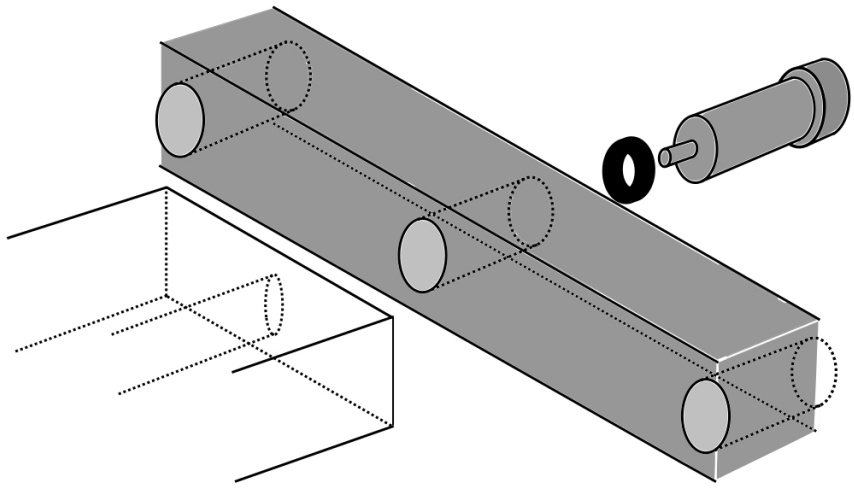

Fig. 3.12. The figure shows a representation of the redesigned pin with 4mm diameter, 1.5 mm thick rubber O-ring. This pin pushed a rubber ring that fit around the oval fibre hole, preventing glue from entering it during layer production.

To assure the contact between the pin pushing the O-ring and the scintillator bar, a push-bar system was used (see figure 3.13). The push-bar consisted of a separate bar of aluminium fixed in along one edge of the frame where pins had been inserted. The push-bar contained grub locator screws that when turned put pressure on each of the 50 pins of their side of the layer. On the other side of the layer, O-rings and pins had already been inserted. Due to the elastic nature of the O-ring, once inserted and under pressure from the opposite end of the bar, the rings expanded beyond the size of the 2 mm radius hole in the aluminium frame. Under pressure the O-ring were held in place and provided a good seal between the frame and bar. The completed system held each bar in place with a 1 ± 0.1 mm gap between scintillator bar and aluminium frame.

With the bars held in place, araldite glue was applied and spread across the layer, then the two 1 m $\times$ 2 m lead sheets were lifted and placed on top. To lift the lead sheets and eventually the completed layer, a suction cup crane was used. The lead sheets were trimmed to fit as closely as possible in order to minimize the gap where they join in the centre of the layer. To provide pressure on top of the lead sheeting, a vacuum system was used. This ensured that the layer was within height restrictions and maximised contact between lead and scintillator. A completed and vacuum sealed layer is shown in figure 3.14.

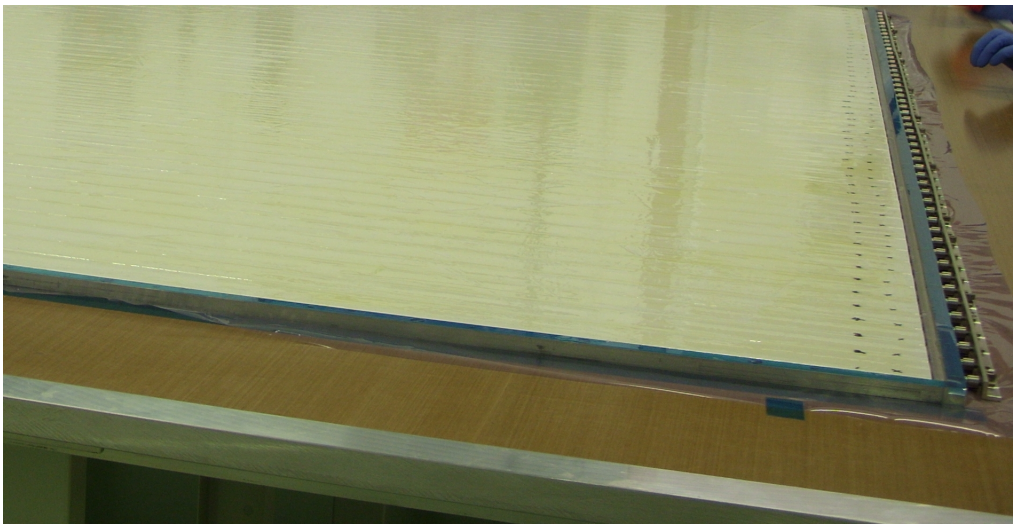

Fig. 3.13. Photograph showing a downstream ECal layer in mid-production. The figure is included in order to highlight the push-bar system, seen here on the far right. Pressure is applied to each locator pin which holds a bar in line with the frame hole and prevents glue from entering the hole during layer production.

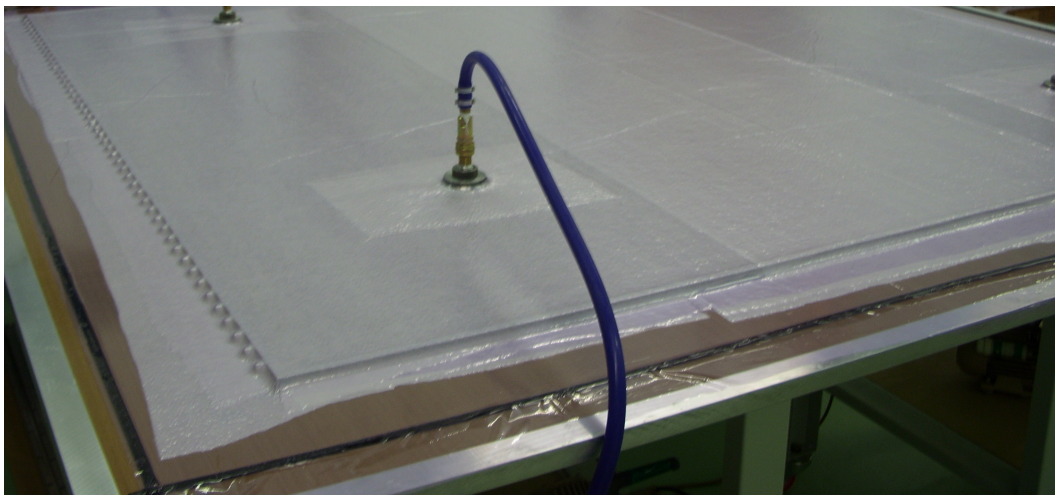

Fig. 3.14. This photograph shows a completed downstream ECal layer which is vacuum sealed in order to provide pressure and ensure good contact between lead and scintillator whilst the glue is drying. The pressure will also ensure that all components are pushed down into place, keeping each layer within height tolerances. Figure taken at Lancaster University by a member of the construction team.

After leaving for a drying time of 12 hours the layer is unpacked and cleaned of any excess glue. This then completes the layer building stage of construction. For the DsECal 34 layers were made in an identical procedure and stored ready for module assembly.

3.3.7.2 Downstream ECal Module Construction

The DsECal is built into an aluminium bulkhead which acts as structural support as well as providing piped cooling for the detector electronics. The first stage of the module build, after the first layer is placed on the aluminium bulkhead, is fitting the detector Light Injection (LI) system. The LI system on the ECal aims to provide a source of known light to test the photon collection and detection of the fibres and MPPCs. The LI system for the ECal is fitted in the 1cm gap between the 2 m $\times$ 2 m layers and the bulkhead wall. To illuminate this area, LEDs that are pre mounted and wired along a 1 cm thick tape are laid on the front and back bulkhead plates next to the first and last layer. Figure 3.15 illustrates the very restrictive space requirements. A cylindrical lens is placed on top of the LED tape. Simulation and testing shows that this lens enables an even distribution of illumination throughout the gap.

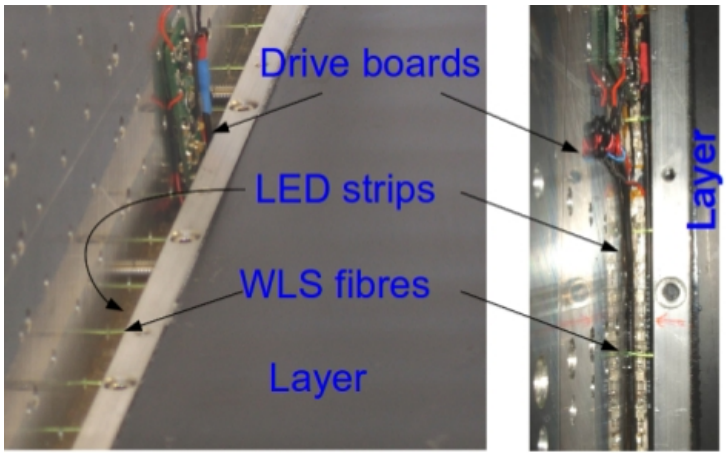

Fig. 3.15. This figure shows the light injection system used in the downstream ECal. The figure shows the components used and the tight space given to fit the light injection system. Image taken from Davies (2011).

With the LI system fitted to the bottom plate, the first layer can be threaded with fibre and tested. As with the MPPCs and scintillator bars, the Wavelength Shifting (WLS) fibre underwent extensive quality assurance (QA) testing before being used in construction. The fibre is inserted by hand through each of the 50 bars in each layer. Once inserted, a plastic ferrule is glued to the end of each fibre to allow secure fitting of each MPPC. The fibre to MPPC coupling is shown clearly in figure 3.16.

After each layer is fitted with fibres and ferrules, the layer is scanned using a 2D robotic scanner. This system uses a mounted Caesium-137 3 mCi (111 MBq) source which is positioned

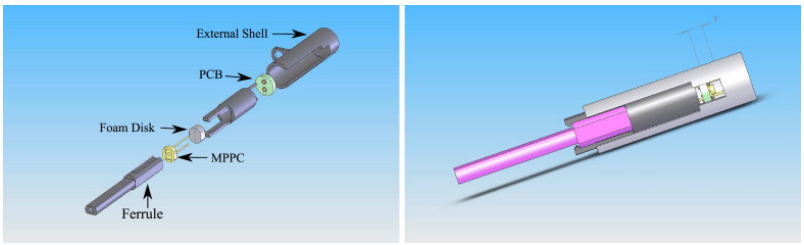

Fig. 3.16. This is a representation of the coupling materials that are used to marry the fibre and ferrule to the MPPC securely. A large challenge in this design was to limit the force applied to the face of the MPPC in order to avoid any damage.

at stages along each bar automatically overnight. At this stage of construction the layer did not have the final MPPCs fitted that would stay in use on each fibre as part of the ND280 detector. Instead 100 test MPPCs of known quality were used to ensure an accurate measure of the integrity of the bar to fibre and ferrule coupling. These MPPCs, as well as the TFB and RMM boards used to read out signals, were identical in design to the final components used in the detector.

Once the layer had been scanned and passed for quality, the next layer was fitted until all the layers were completed. The next and final stage was the fitting of the MPPCs and the wiring of each to TFB boards mounted on an outer aluminium container. With all 3400 MPPCs wired to TFBs, the module was complete. It was then shipped to CERN in Geneva to undergo extensive testing using cosmic data and a controlled test beam.

3.3.8 Side Muon Range Detector, SMRD

Charged Current Quasi-Elastic (CCQE) muons created at large angles close to perpendicular to the beam direction cannot be easily measured by the TPC. Whilst meaningful information can be gained from observations in the ECals, in order to provide accurate ranging observations, detection material was placed inside the ND280 magnet return yoke. This is what makes up the Side Muon Range Detector (SMRD). As well as detection of high angle CCQE muons, the SMRD will also provide accurate detection of cosmic muons both for cosmic triggering and for vetoing Minimum Ionizing Particle (MIP) tracks in triggered beam events.

To provide a magnetic field, the ND280 makes use of the recommissioned UA1 magnet. The magnet consists of water cooled aluminium coils, which create the horizontally orientated dipole field, and a flux return yoke. This in part can be seen in figure 3.7. Each side of the magnet return yoke contains 8 sections which contain 17 mm air gaps. The SMRD utilises these

air gaps by placing a scintillator, fibre and MPPC set up constructed from similar materials to those used throughout the ND280 detectors. In contrast to the relatively fine-grained inner sub-detectors, the SMRD used scintillator slabs. Each of these measuring $870 \times 170 \times 10$ mm^3 and $870 \times 180 \times 10$ mm^3 for the horizontal and vertical gaps respectively. The fibre is installed in a wave like groove across the bar and uses read-out on both ends provided by the same Hamamatsu MPPC devices used throughout the ND280 detector. This is shown clearly in figure 3.17.

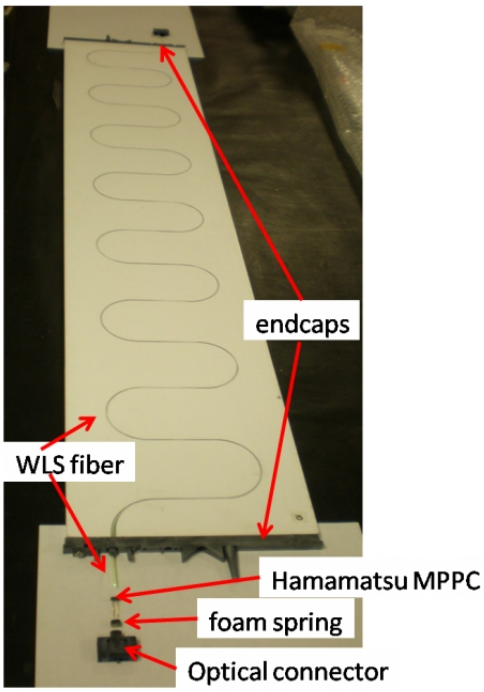

Fig. 3.17. This figure shows an image of the scintillator bar, fibre and MPPC set up used in instrumenting the magnet and creating the SMRD detector. The image clearly shows the differing fibre scintillator coupling used here in comparison to all other scintillator based detectors used in the ND280. This wave like scoring was used to increase the efficiency of using the much wider SMRD bars.

Due to financial restrictions, all gaps in the magnet could not be instrumented. The decision on which to implement was centred on how best to fulfil the SMRD's aim. As such the downsteam sections were favoured. This was due to the interest in the forward moving tracks emanating from neutrino events in the ND280 fiducial volume.

3.4 Super-Kamiokande Far Detector

Super-Kamiokande (SK) is a water Cherenkov detector built in Kamioka's underground observatory close to the west coast of Japan. Super-Kamiokande is an upgraded version of the

original Kamiokande detector which was first built in 1983 and designed to study nucleon decay. This gave the detector its name, Kamioka Nucleon Decay Experiment, or KamiokaNDE. Although originally designed to study nucleons, it gained its fame from the observation of neutrinos from supernova SN 1987A (Hirata et al. (1987)) and later from solar and atmospheric neutrino studies. In 1995 it was decided that a larger detector with greater precision was needed.

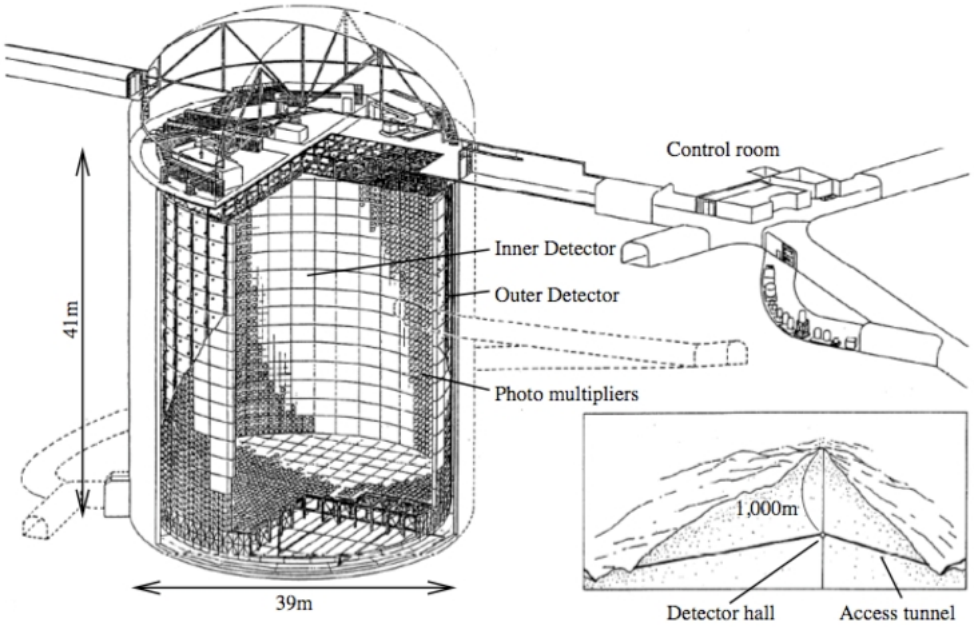

Fig. 3.18. This figure shows a representation of the Super Kamiokande water Cherenkov detector. The PMT instrumented inner and out detectors can be seen, as well as the electronics and servicing superstructure. Image taken from T2K (2013).

Super Kamiokande now contains 50,000 tons of ultra pure water contained in a 41.4 m height, 39.3 m diameter cylinder surrounded by 11,200 50 cm diameter PMTs. It is located in Mozumi Mine and acts as the far detector for the T2K experiment. Mozumi mine lies under Mount Denoyama and is approximately 1 km underground, which means that the detector hall is shielded from cosmic muons with energies up to 1.3 TeV. As with all neutrino observatories, SK detects the charged particles created during neutrino decay. This observation is made through observation of the Cherenkov radiation emitted as the charged particle travels faster than light in the dielectric pure water fiducial volume. The Cherenkov radiation is emitted as a cone of light with an angle such that

$$\cos\theta_c = \frac{1}{n\beta} \tag{3.1}$$

Therefore the radiation is emitted in a cone of half-opening angle θ_c, this can be seen in figure 3.19.

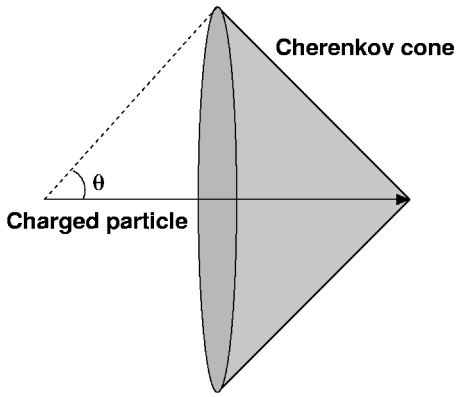

Fig. 3.19. A Cherenkov cone with half-opening angle θ. The charged particle is travelling from left to right.

This cone of light is detected by Hamamatsu Photo Multiplier Tubes (PMTs). Super Kamiokande is split into inner and outer detectors, both instrumented with PMTs. The sectioning of these detectors can be observed in figure 3.18. The outer detector's main purpose is to highlight and veto any inward coming cosmic muons that act as a background to neutrino interactions in the inner detector.

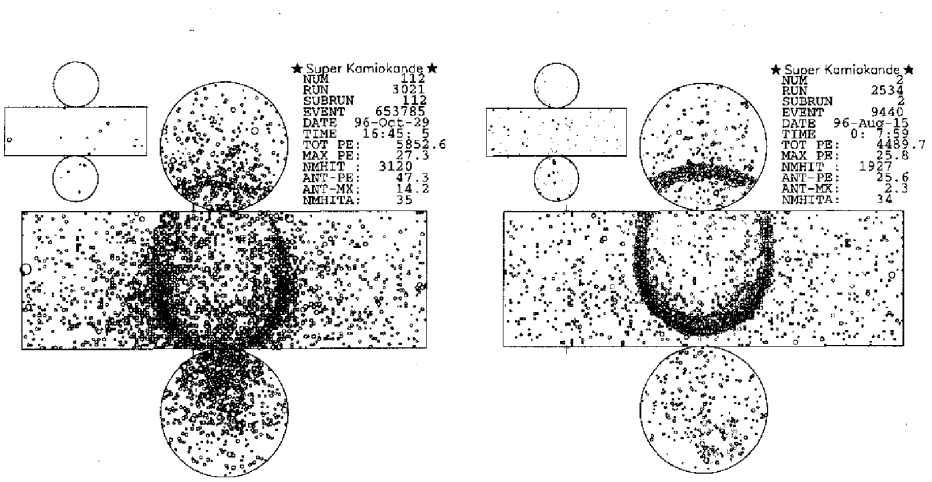

Fig. 3.20. Charged current interaction event displays for an atmospheric ν_e (left) and an atmospheric ν_μ (right) in Super-Kamiokande. The main central view is from the inner detector volume. The outer volume view is shown in the upper left corner.

Observations of the Cherenkov cone allow the measurement of the direction and energy of the produced charged particle as well as particle identification. Figure 3.20 shows an event display of a positively identified atmospheric ν_e and ν_μ. Identification of both ν_e and ν_μ will come from studying reconstructed electron and muon rings. Electrons, as seen in the left image in figure 3.20, deposit energy in a fuzzier ring in comparison to the muon ring on the right. This is due to the minimally ionising nature of a muon passing through the detector, which is in contrast to the path taken by the electron with its shorter radiation length.

Chapter 4

ND280 Software

The ND280 software is a set of packages which are designed to analyse all aspects of the experimental data. It is predominantly written in C++ and Python, and makes use of many packages designed for high energy physics.

The software is split into two types, online and offline, with each name based on its use in the experiment. Online software is responsible for collecting the data and recording it into a readable format ready for analysis. The offline software is run on the raw data recorded by the online software and is responsible for calibration, reconstruction of physics objects and their analysis. Throughout my time with the collaboration, I helped document and design a number of packages in the offline software. My work was predominantly focused on the reconstruction of objects inside the Tracker ECals.

4.1 Online Software

The online software can itself be split into two categories. The Data Acquisition Software (DAQ) is tasked with interfacing with the ND280 electronics and creating a readable format for the offline software. The second online software package is the Global Slow Control, or GSC. The GSC package monitors each sub-detector by storing monitoring histograms that track monitoring variables during detector operation. This monitoring is vital in taking validated data. Both packages are run simultaneously and make use of the MIDAS software framework (Ritt et al. (2013)). The author's understanding of the online software comes through study of the T2K Nuclear Instruments and Methods Paper (Abe et al. (2011c)), as such some of the descriptions here could be similar to the cited source.

4.1.1 Data Acquisition Software

The DAQ collects and records data passed to it from each sub-detector's front end system and stores the collected information in data files. The complete DAQ and GSC framework is shown in figure 4.1.

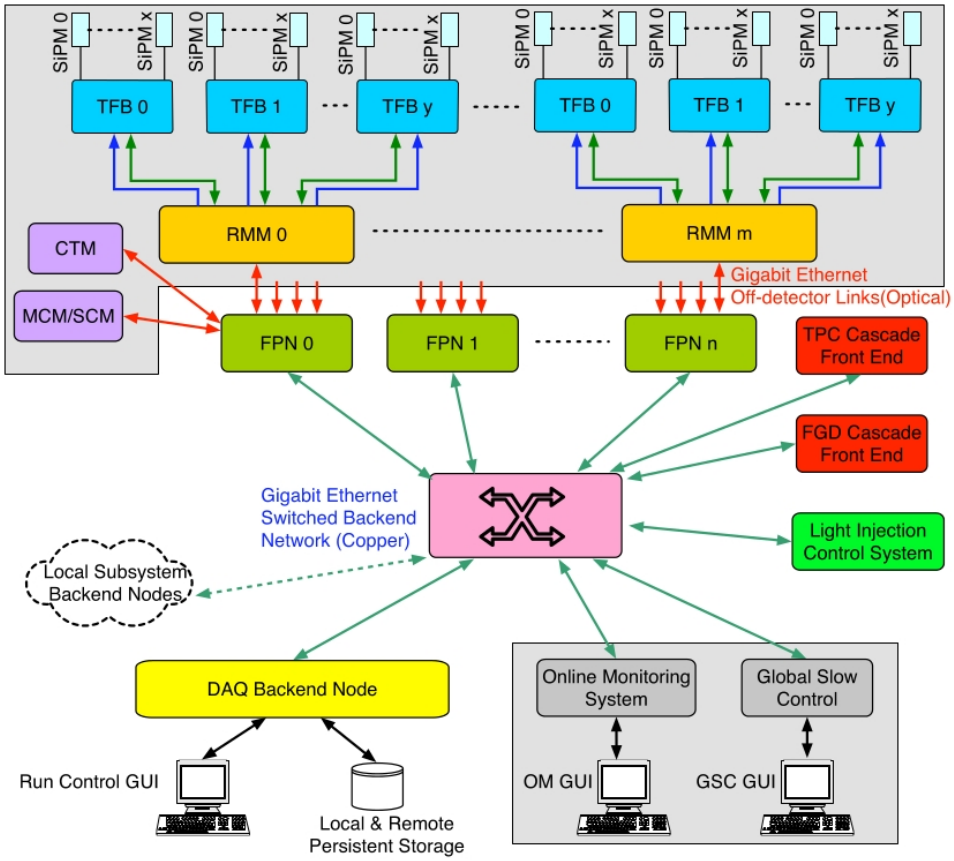

Fig. 4.1. This figure is a representation of the framework for the DAQ and GSC software. Included here are; TRIP-t Front-end Boards (TFB), Read out Merger Modules (RMM), Cosmic Trigger Module (CTM), Master Clock Module (MCM), Slave Clock Module (SCM), Front-end Proc. Node (FPN). The image is taken from Abe et al. (2011c).

This framework shows the interface between TFBs of the Trip-t based sub-detectors, RMMs and the Front End Processor Nodes (FPNs). The FPNs seen here service up to 2 RMMs each. Each part of the framework is connected by point-to-point Gigabyte Ethernet cables. A Read-out Task, or RXT, provides configuration and retrieval from the electronics. This includes both hit information as well as monitoring data for the GSC. The RXT is parallelized across the boards with the data buffered for access by the Data Procession Task or DPT. The DPT performs a number of tasks including applying timing and charge amplitudes for hits and performing pedestal subtraction and zero suppression for each channel. If triggered, the DPT also performs histogramming prior to zero suppression.

There are four Trip-t based sub-detectors in use in the ND280 pit; the P0D, ECal's and SMRD within the ND280 and the separate INGRID sub-detector. The remaining TFB and FGD detectors do not make use of Trip-t electronics. These are read out separately by differently configured instances of MIDAS, which feeds data into the global DAQ in parallel to the data

from the Trip-t FPNs. For further information on how the DAQ handles the non Trip-t detectors see the T2K NIM paper (Abe et al. (2011c)).

After data collection, the MIDAS DAQ buffers data to a RAID array. This array is then archived both off-site and at a local storage server than can be accessed for quick analysis. This locally stored data was used extensively during commissioning and early calibration.

4.1.2 Global Slow Control

The GSC is run on two computers in the ND280 control room. These computers produce online web pages which can be used to monitor each experiment. Each detector can also set off alarms on important attributes recorded in the GSC. These online monitoring pages and alarms are used extensively during safety shifts that are run as part of all ND280 data taking shift work. The data collected is stored in a central database named the online database (ODB) and then transferred to a MySQL database at a rate of 0.5 Gb a week. This database and an electronic log (Elog) that is written during data taking shifts are stored at both the detector site at J-PARC and at TRIUMF laboratory in Canada.

4.2 Offline Software

The offline software is responsible for the calibration, reconstruction and analysis of data, and the simulation of interactions and electronics. The packages will be described as they were at the beginning of 2010, when the author finished the last of the analysis he was tasked with. At this time, packages were still in development and they did not represent a final product. Further to this, they were often yet to meet the precision specified in the design documents.

4.2.1 Simulation

The simulation software for the ND280 can be split into four sections. The first is a beam generator which models the creation of neutrinos starting with the proton beam colliding with the graphite target and concluding with meson decay in the decay chamber. The next simulation package models neutrino interactions, outputting the products of these interactions inside the detector. The detector itself is then simulated, modelling the detector and how particles propagate and decay within it. Finally the electronic response of each detector is simulated. The output of these simulator packages will mirror the data output in format. This allows calibration,

reconstruction and analysis packages to be run over both simulator data and real data reliably, whilst offering consistency in analysis.

4.2.1.1 Neutrino Interaction Generation

The ND280 software was designed to be neutrino interaction simulator agnostic. However two neutrino simulator packages have been used in preference to others during the author's time with the ND280 experiment: NEUT (Hayato (2009)) and GENIE (Andreopoulos et al. (2010)). Each of these generators took input from the neutrino beam Monte Carlo which contains n-tuples describing the neutrino energy, direction and position. The generators use this information with a ROOT based geometry to model the neutrino nucleon interactions. These interactions are modelled by weighting and simulating intra-nuclear interactions using physics based estimations and, where available, real world observations.

4.2.1.2 Detector Simulation

The nd280mc package is responsible for building a simulated version of each subdetector. This is achieved using a ROOT based GEANT4 software library (Agostinelli et al. (2003)). As previously stated, this model of the detector is used as an input in neutrino generation. It is then used again when simulating the propagation and decay of products from those neutrino interactions and other simulated interactions such as cosmic background events. This simulation is performed by GEANT4 run inside nd280mc. GEANT4 will return a series of energy deposits in detection material. Each detailing the amount of energy deposited in each material. In addition nd280mc is used extensively in testing reconstruction packages through use of a particle gun feature. This allows the production of any particle over an energy range at set positions and angular spread. This has proved to be a vital tool when evaluating energy and spatial resolutions.

4.2.1.3 Electronics Simulation

The electronics simulation (elecSim) is the final stage of the simulation chain. This package takes the output from nd280mc giving the amount of energy deposited in each region and applies a number of simulated effects to 'un-calibrate' the energy deposits in order to mimic real world electronics responses. These include ion drift and Micromegas responses in the TPC; light attenuation along scintillator bars and WLS fibre; noise and MPPC responses in the scintillator based detectors; and a simulated response of the TPCs and other front and back-end electronics.

The final product of this is a series of objects called ‘digits’. These digit objects are identical to those used to output data from the DAQ.

4.2.2 Calibration Software

The calibration software is tasked with taking the simulated or real world digits and outputting ‘THits’. These hits represent a deposit of energy or charge at a calibrated time in a labelled detection medium. Inside this package, channel by channel calibration will be applied to remove a number of effects.

TPC calibration first applies a linearity correction that, using data recorded in a charge injection run, normalises the response of the detector. In addition the TPC must also apply corrections arising from differences in gas density. This produces a time dependent effect and is corrected through observations of two ‘mini-TPCs’ and cosmic events. The mini-TPCs use the same gas supply but are each fitted with a known radioactive source at a known distance. With data collected from the mini-TPCs and from partially reconstructed cosmic data, the TPC can calibrate out the effect of any Micromegas to Micromegas differences as well as the effects of varying gas density.

The calibration of scintillator and fibre based detectors once again starts with a normalising linearity correction. This correction is based on data from charge injection runs that make use of the ability of the TFBs to inject a known charge into each channel. Following this, a number of MPPC based effects must be calibrated out. Calibration of noise and saturation based effects is based on work done during test bench studies (Vacheret et al. (2011)) and bar to bar responses are monitored using understood cosmic tracks which are reconstructed later in the software chain. Here a known MIP deposit produced by a cosmic muon is compared across bars in order to study varying efficiencies.

The final stage in calibration is actually performed during reconstruction. This stage corrects the energy lost due to attenuation effects of the bar and fibre. The author worked in conjunction with the team that implemented the first pass attenuation correction for the downstream ECal. A more detailed description for the attenuation corrections applied to the Tracker ECals is given in section 4.2.4.

4.2.3 Reconstruction

The initial reconstruction of physics objects is performed by individual packages for each subdetector. Each subdetector reconstructs with just the observations made in its detection material, with the exception of the FGD and TPC which were combined early on in order to more accurately reconstruct vertices. The final design for reconstruction was to combine the reconstructed objects and associated likelihoods outputted by each reconstruction package. The combination of reconstructed objects was to be performed by a 'global' reconstruction package which would fit each of the objects together based on the likelihoods provided. This however had yet to be fully implemented during the author's time with the experiment (ending summer 2010). At this time analysis was performed using the output of each individual reconstruction package rather than a global object.

The reconstruction of the Tracker region will be discussed in more detail here as it is relevant to the author's work included in Chapter 6. This will include a brief description of the reconstruction and particle identification performed in the TPCs and FGDs. There will be a more rigorous description of ECal reconstruction in section 4.2.4 due to the author's extensive experience with the software.

TPC and FGD reconstruction first starts with analysis of hits produced in the TPCs. These hits have an accurately known position in 3 dimensions, with a resolution of the order 1mm (varying with incident angle and drift distance). These TPC hits are then grouped into clusters of hits with similar positions and times. From these clusters the reconstruction builds tracks that describe a particle's trajectory. The tracks are then extrapolated into FGDs and 3D reconstruction of FGD tracks is applied. This stage is made much easier with the well known track position in the TPC allowing the 3D matching of two 2-dimensional tracks in each of the FGD bar orientations. Importantly the FGD can provide accurate timing information for the track; this would otherwise be unavailable if the track did not pass a central cathode.

In addition the FGD also runs a separate reconstruction of the remaining hits that may have been made by particles that do not propagate through the TPCs. This requires independent 3D matching that is achieved by comparing the shape of the tracks and timing information.

The particle identification (PID) in the TPC is done through measuring and analysing dE/dx using the momentum of the particle's track calculated through studying its curvature. The mean value of dE/dx is plotted against the track momentum. This is then compared to expectation for various particle masses.

4.2.4 ECalRecon

The ecalRecon software package is responsible for the initial reconstruction of physics objects in the tracker region's calorimetry. These physics objects are formed from hits (charge deposits). They are recorded during data taking from the calorimeter's photo-detectors (MPPCs) or from a simulated response as part of the electronics simulation. The hits include a calibrated time in nano-seconds, a measure of the amount of charge recorded in photo-electrons, and a location ID.

The package is structured around a central class that controls the running of algorithms. This algorithm chain is illustrated in figure 4.2.

4.2.4.1 Hit Separation and Sorting

The first task in ecalRecon is the separation of the hits from each ECal sub-detector in real or simulated time bunches. In accordance with the bunch structure from the proton ring (see section 3.1), each bunch of hits is defined as have a separation of 50 ns from the next bunch. Hits with non-physical times or charges resulting from failed calibration are also sorted and labelled at this stage.

Timing is a valuable tool in reconstruction and is used extensively throughout. Any given neutrino must be associated with exactly one of the six bunches produced by the accelerator, so in general only hits from a specific bunch are likely to arise from a single interaction. The principal exception to this is Michel electrons from muon decays at rest, which will be delayed by τ_μ and are generally associated with a later bunch. A Michel electron tagging method, which looks for low-energy electron showers, has been developed to handle this.

4.2.4.2 MIP Equivalent Charge Units and Early Attenuation Correction

The majority of methods in the ECal reconstruction make use of a MIP equivalent measure of energy deposited, where one MIP equivalent unit (MEU) is the mean energy deposited by a minimally ionising particle MIP passing perpendicularly through a scintillator bar. The reason to use this unit is purely the simplicity of obtaining this energy measure in calibration. The conversion of the charge given by the calibration in photo-electrons (pe) to the MIP equivalent unit is done in two stages. First the charge in pe is converted to a reconstructed number of incident photons on the MPPC. The 3rd degree polynomial used in this conversion is given below.

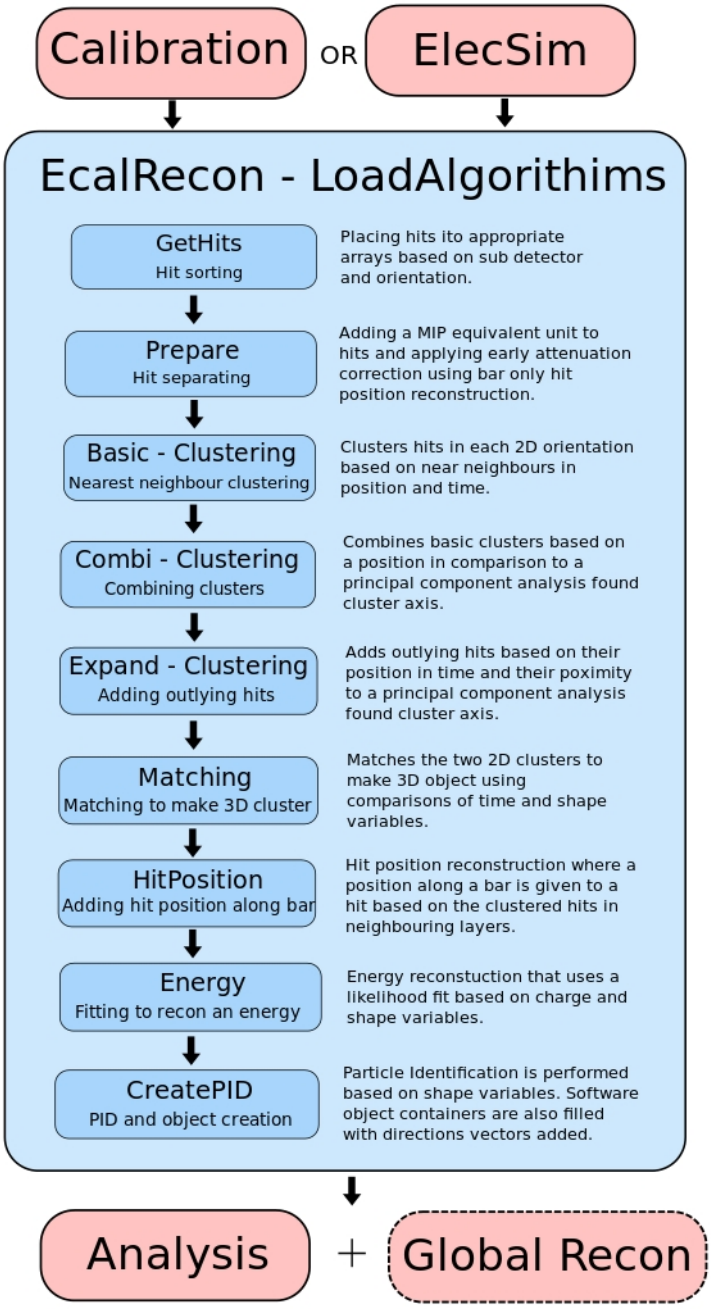

Fig. 4.2. The structure of ecalRecon including its algorithm chain.

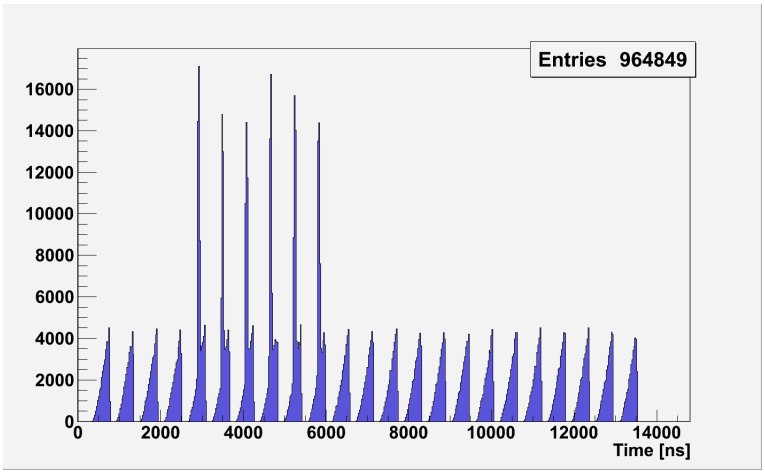

Fig. 4.3. This plot shows clearly separated time bunches in the test beam data.

$$\text{Number of incident photons} = A_1 + A_2 Q + A_3 Q^2 + A_4 Q^3 \tag{4.1}$$

Here A_1 = -4.48751, $A_2 = 5.05916$, $A_3 = 2.06835 \times 10^{-3}$, $A_4 = 4.01170 \times 10^{-6}$ and Q is charge in units of pe.

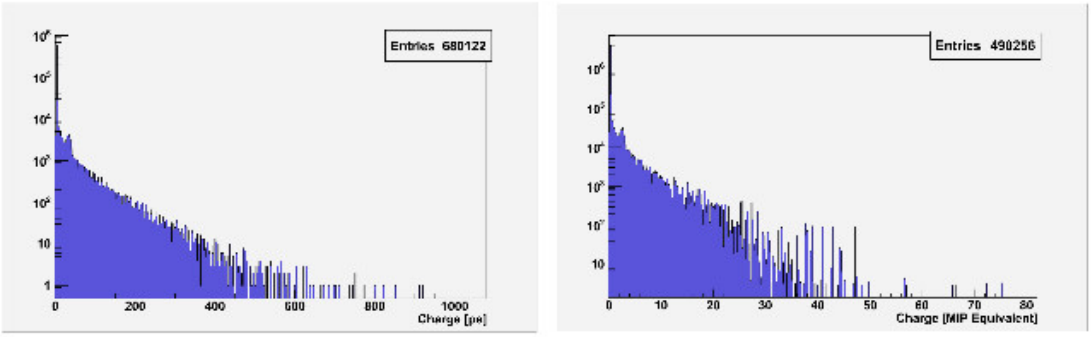

Fig. 4.4. These figures show the charge deposited in ECal MPPCs by the same objects. The left is recorded in photoelectron units and the right plot uses a MIP equivalent unit.

The reconstructed number of photons is then converted to MIP units and an attenuation correction is applied. The application of an attenuation correction for light lost as it travels down a bar will require some estimation of the initial charge deposit location. To achieve this, where possible and within a time cut, hits from both ends of the scintillator bar are combined. These hits are then used to reconstruct a position along the scintillator bar. This position is calculated

using the ratio of charges and times of the two hits. Shown in figure 4.5 is the resolution of both the charge and time comparison method. When information from the one end of the bar is not available, the centre of the bar is used as the best estimate of hit position.

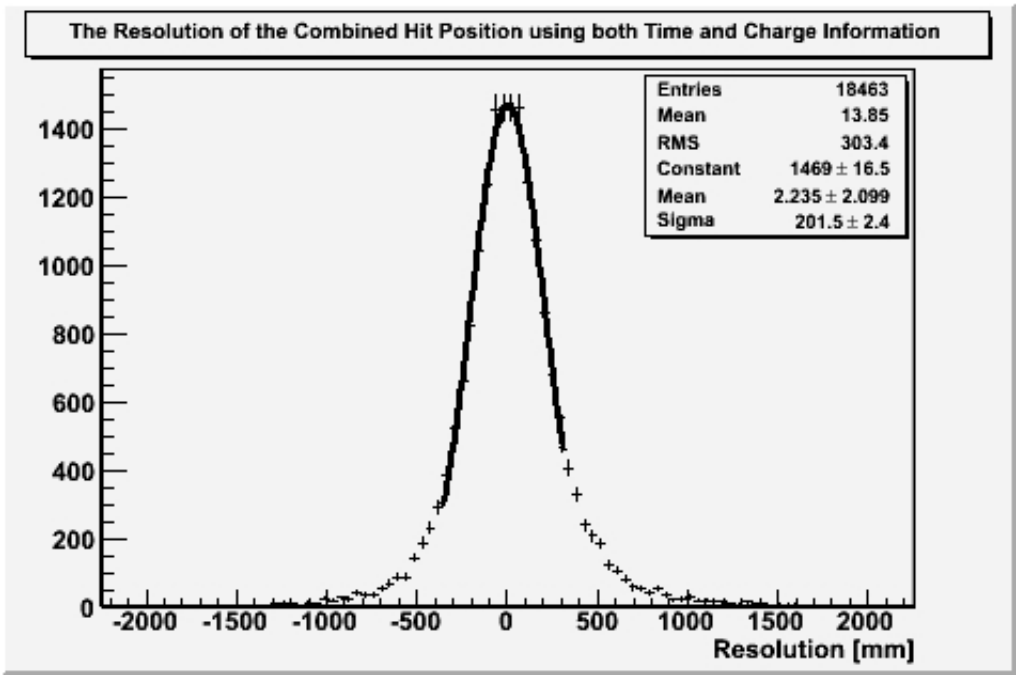

Fig. 4.5. A plot showing the fitted position minus the true position of the early hit position reconstruction in the ND280 Tracker Calorimetry. The data used is a selection of cosmic events collected in the Downstream Calorimeter whilst the detector was in situ in the ND280 Pit.

This is the first of two position reconstruction techniques used in the ECal hit reconstruction. The second in most cases is more reliable. Even with the incomplete coverage of possible position reconstruction at this early stage, it is still of benefit to have improvement in our charge measure. The reason for this is the importance placed on the ordering of hits by their charge in the next stages of object reconstruction.

The attenuation parameters are calculated using straight tracks seen in cosmic data collected in the downstream ECal. The attenuation profile of the wavelength shifting fibre used in the production of the ND280 ECals has been studied at many stages in the production and is found to fit to a double exponential function referring to ‘long’ and ‘short’ attenuation components. These are thought to arise from attenuation of light in the central body of the fibre and from light trapped in coating or cladding around the fibre.

Through MC studies it has been estimated that the MIP unit refers to an energy deposit of approximately 2.4 MeV.

4.2.4.3 Clustering, Noise Filtering and Matching

With the hits now combined with relevant partners and their time and charge as accurately calibrated as possible, the task of combining hits into groupings of associated objects begins. These objects are described as either a track, created by a MIP-like particle or a shower, created by multiple interactions and products of electromagnetic or hadronic particles.

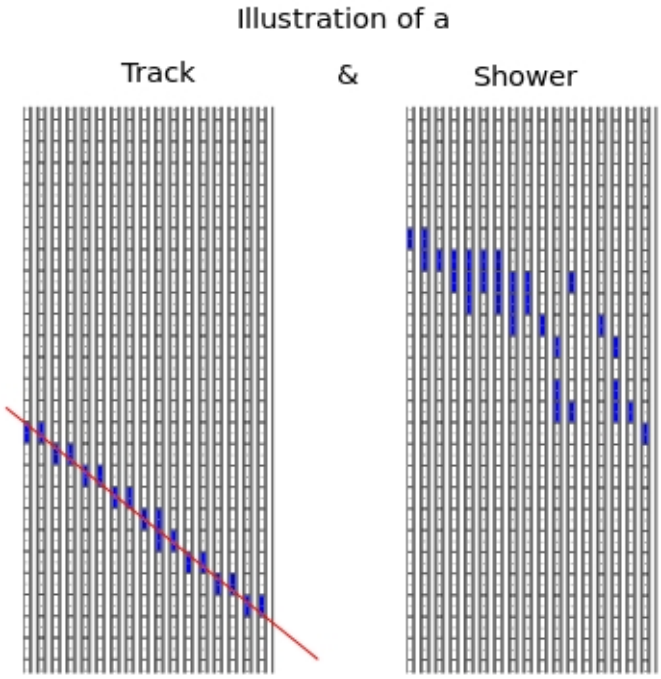

Fig. 4.6. On the left is an illustration of the track left by a minimum ionising particle travelling through layers in the DsECal and on the right, an electromagnetic shower.

The combination of the hits into objects is done in two clear stages. The first stage, 'Clustering', groups neighbouring hits in each of the ECal's two-dimensional frames into 2D objects; the second, known as 'Matching', combines a pair of 2D clusters into a single 3D object. Following this the two 2D objects are combined to create one 3D object; this secondary stage is termed in the ECal Software as 'Matching'.

The clustering stage begins by grouping hits which are close geometrically and temporally. This is achieved initially by looking for neighbouring hits around a high charge hit. If a hit is found in either of the bars next to or in a similarly orientated layer in front or behind this hit they are grouped together. If three or more hits are grouped, they are kept and form a small cluster.

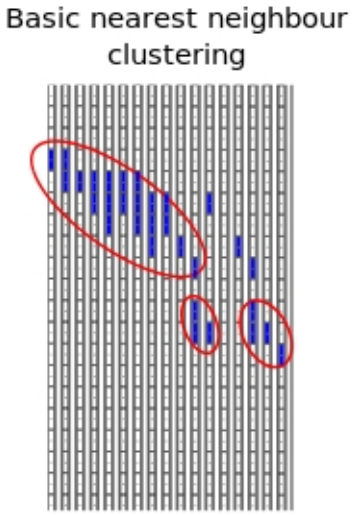

Fig. 4.7. This shows the shower from figure 4.6 with the red circles enclosing hits which would be grouped and kept as small clusters using the basic nearest neighbour clustering method.

Related small clusters must now be combined to form larger objects. This is done by comparing the largest cluster with those around it. This comparison is done through the use of Principal Component Analysis (PCA) (Jolliffe (1986)). This tool, when used to analyse a two-dimensional object, describes a pattern as two vectors, a length and a width.

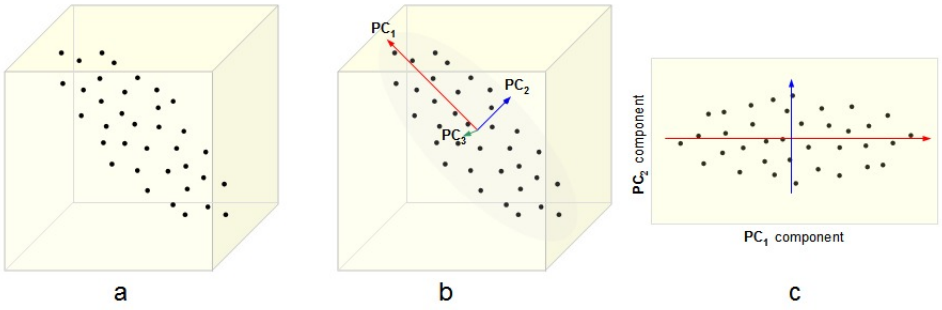

Fig. 4.8. An illustration of principal component analysis. Diagram a) shows a data set given as 3-dimensional points. The three orthogonal Principal Components (PCs) for the data are shown in b) and are ordered by variance; c) shows the projection of the data set into the first two PCs, discarding the third one (Kavraki (2007)).

The length vector of the master cluster is then used to define an axis of the clustered object. The neighbouring clusters are compared through three cuts to the master cluster and its axis. These cuts are:

- The hits in the cluster must be within 40 ns of the master cluster.
- The cluster must have a similar length vector component.
- The cluster centre must have a perpendicular distance from the master axis of less than 80mm.

If these cuts are passed, the hits in the satellite clusters are grouped with those in the master cluster. The next and final stage of clustering aims to pull any satellite hits missed by the first stage back into our master cluster. These small groupings of hits are often created by some form of large angle scattering of a small part of a shower or an electron produced by ionisation as a MIP traverses the detector. In the case of showers, these hits prove very important in finding the direction and energy deposited by the shower through use of shape comparison. Adding these hits to a track object however often proves detrimental to the PID of the track, with these off-shoot hits adding only confusion from the typical and expected straight object. The addition of these hits is done by once again making use of the PCA tool. The hits are given a likelihood of inclusion associated with an oval created around the master cluster using the components of the PCA. If passed they are included completing the formation of our 2D clusters, with any extra hits being put into an unclustered hit container.

The next task is to combine two clustered 2D objects to form a 3D object. This can become very difficult depending on the number of 2D objects and the angle at which the particle entered the detector. Investigation of the matching stage has been relatively limited compared to other stages of the reconstruction and is in fact the focus of current unconcluded studies. The method used in the software at the time of this research compares a number of shape and time variables. This comparison is done by creating a likelihood-like rating that is used to rate the similarity of two 2D clusters. The variables compared are; front, middle and back cluster position, total charge of clusters, and direction (first eigenvalue of PCA).

In the majority of cases, the ‘matching’ has an easy job. With only one object typically passing through each ECal inside one of the bunch windows, there should only be two clusters to match that it should put together to form the 3D object. Difficulty comes when two objects fall inside the same detector in the same bunch window. In this case the above cuts are relied upon to fit the correct cluster.

4.2.4.4 Hit Position Reconstruction

With the matching complete, a 3D cluster is now formed. This allows improvements to the reconstruction of positions of hits along each scintillator bar through study of the adjacent layers. An improvement in the hit positions is important at this stage as it allows for a second, and more accurate, estimation of the charge lost through light attenuation. The improved calibration is used in the next step in the reconstruction of ECal objects, the energy reconstruction. This estimates the energy of the particle that enters the ECal, making use of the calibrated deposit in each hit.

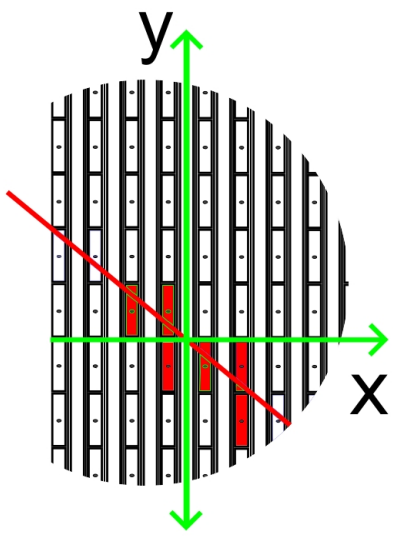

Fig. 4.9. The red line in this diagram shows a best fit line through adjacent orthogonal layers found using a least squares fit analysis.

This hit position reconstruction method makes use of a least squares fit analysis. This finds a best fit line through adjacent orthogonal layers, illustrated in red in figure 4.9.

This line is given by

$$y_i = mx_i + c \tag{4.2}$$

where y is the charged-weighted mean position in neighbouring layers, x is the layer depth, m is the gradient and c is the intercept.

The solution for the gradient and intercept is

$$m = \frac{\Sigma x_i y_i - \Sigma x_i \Sigma y_i}{N\Sigma x_i^2 - (\Sigma x_i)^2} \tag{4.3}$$

$$c = \frac{N\Sigma x_i^2 \Sigma y - \Sigma x_i y_i \Sigma x_i}{N\Sigma x_i^2 - (\Sigma x_i)^2} \tag{4.4}$$

The fit is made for two orthogonal layers either side of the investigated bar, with the reconstructed position being the solution for y at the investigated layer depth. The first and last layers are treated differently as they do not have the requisite layers on both sides. In these cases, only the layers on one side are used.

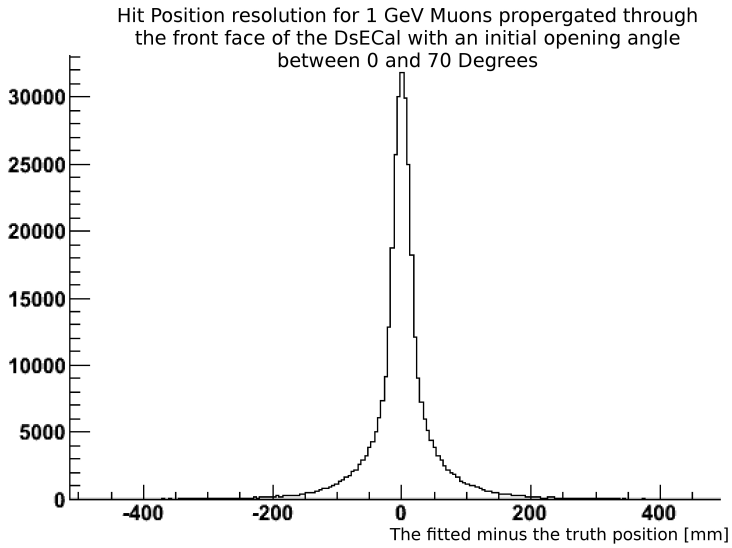

Fig. 4.10. The plot shows the relative low fitted position minus the true position obtained when the 3D ECal hit position reconstruction is performed on straight MIP-like tracks.

This tool is very reliant on good clustering and matching and can produce poor resolutions for objects that are more challenging to reconstruct, such as large or multiple shower events in each ECal. The performance can be improved by making use of the bar-only position reconstruction, detector-wide fitting and second pass, post PID reconstruction.

4.2.4.5 Energy Reconstruction

Energy (or momentum) reconstruction throughout the Tracker region is shared between the TPC and ECal. The TPCs reconstruct the momentum of charged particles through the curvature of the charged track in the magnetic field. In addition, the TPCs can provide particle

identification through measurement of dE/dx. The ECals reconstruct the energy of electrons and photons through the energy deposited in the scintillator. The ECals can also provide particle identification through multivariate analysis of cluster shape variables. This is particularly useful where the TPC dE/dx analysis does not result in a clear identification.

To perform the energy reconstruction, a likelihood function of various charge based characteristics of the object is employed. The parameters currently in use in the reconstruction are:

- Total charge
- The RMS of the charge distribution
- The mean of charge distribution
- The maximum charge in the distribution

The addition of geometry based parameters was investigated and it was concluded that their benefit was limited because high angle clusters pull the fit to incorrect conclusions.

Each of these parameters is found to be well described by a skewed Gaussian. The mean, skew and standard deviation of these distributions are then found over a range of energies and these distributions are used to create a correlation matrix. Expanding the inverse of this matrix through combination with a vector defined as the difference of a variable with its mean will allow the extraction of a probability. This probability can be used now to create a log likelihood function for a range of energies.

Taking the minimum of the inverted likelihood will yield the estimated energy returned from this stage of the reconstruction.

4.2.4.6 Particle Identification

It should be noted that the ECal PID described in the following section is based on the software in 2010. This package in particular has seen large improvements since this point. The ECals offer the ability to identify and study charged tracks and showers. This ability to identify objects as track-like or shower-like in the ECal is of great importance and is the focus of the ECal PID. These labels will help to identify the differences between charged tracks seen in the Tracker region, as well as highlight photon deposits not seen in the Tracker. Through the comparison of parameters that characterise the object's shape and charge deposition, a decision on the object's track-like or shower-like appearance can be made. The algorithm returns a variable centred on

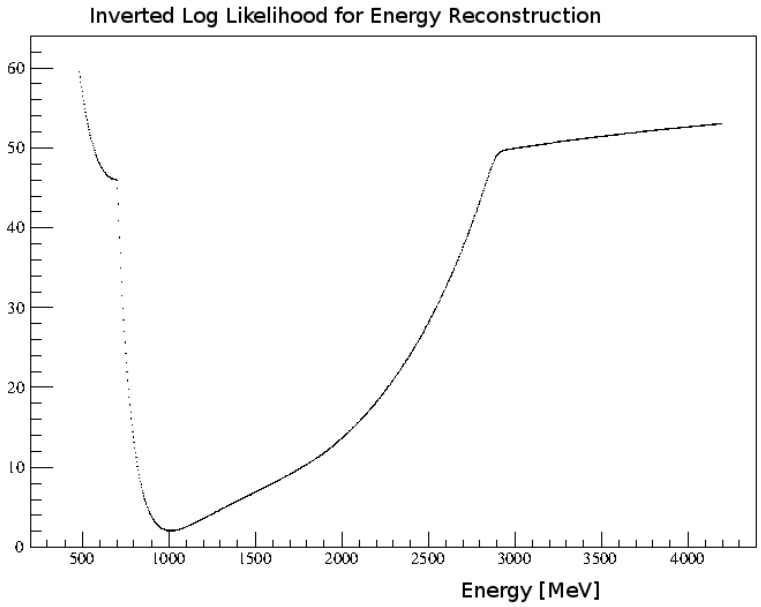

Fig. 4.11. The plot shows the inverted log likelihood function produced when analysing 1 GeV simulated photons passing through the DsECal. The minimum seen here is consistent with this simulated particle. This plot was made by N. McCauley, Liverpool University.

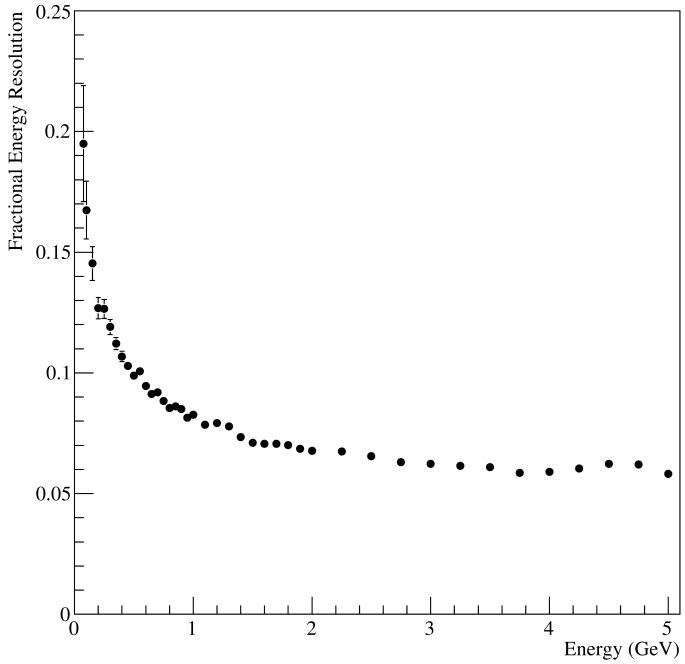

Fig. 4.12. A plot showing the fractional resolution, $\Delta E/E$, of the Tracker ECal energy estimator applied to a sample of simulated 1 GeV photons. This plot was made by N. McCauley, Liverpool University.

0.5 and running approximately between 0 and 1; 0 being shower-like and 1 being track-like.

This comparison is done through the use of a neural network implemented by the Root TMVA tool (Hoecker et al. (2007)).

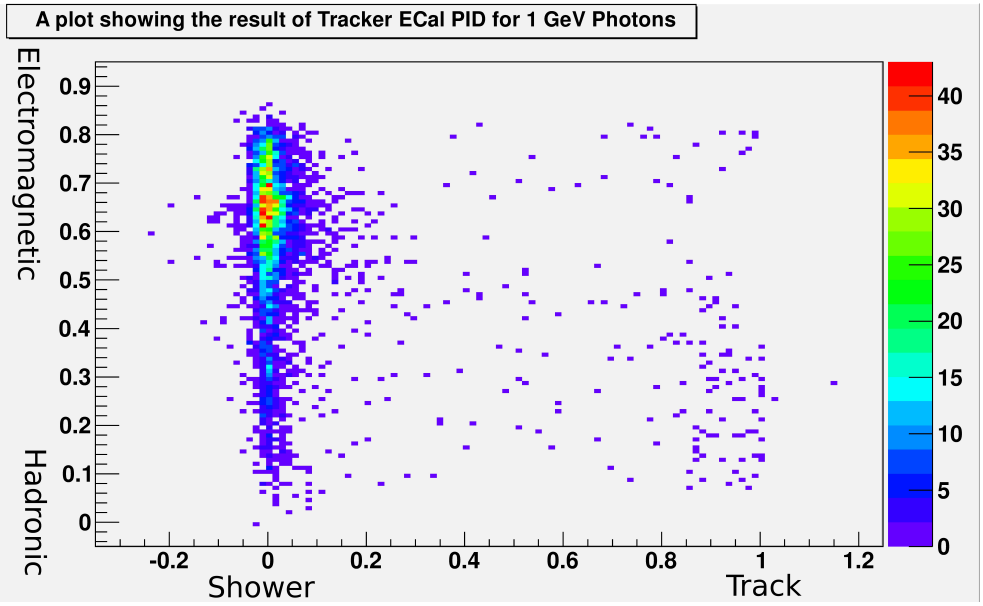

Fig. 4.13. This plot shows the PID output when run over 5000 simulated 1 GeV photons incident on the front face of the DsECal. Each photon is simulated with a random incident angle of up to 70 degrees from the beam axis. The 2D plot shows the output from both the Track vs Shower decision and the Electromagnet vs Hadronic decision. The plot clearly shows the favoured Electromagnetic Shower decision, the expected outcome for 1 GeV photons.

Figure 4.13 and 4.14 provide examples of how the PID could be used to provide particle identification using data gathered only by the calorimetry. In future, particle identification in the Tracker region will be optimised by combining PID information from all available sub-detectors.

For additional information in the design and implementation of the PID tool during this thesis period, see Carver (2010).

4.2.4.7 Shower and Track Fitting

In this final stage of the reconstruction, the finalised and outputted objects must be constructed. This involves fitting of any attributes needed in their study or combination with other objects seen throughout the wider detector. This includes direction fitting, which makes use of a PCA analysis very similar to that used in the 3D hit reconstruction. Figure 4.15 shows the performance of the Tracker ECal only direction fitter during the testbeam commissioning of the DsECal.

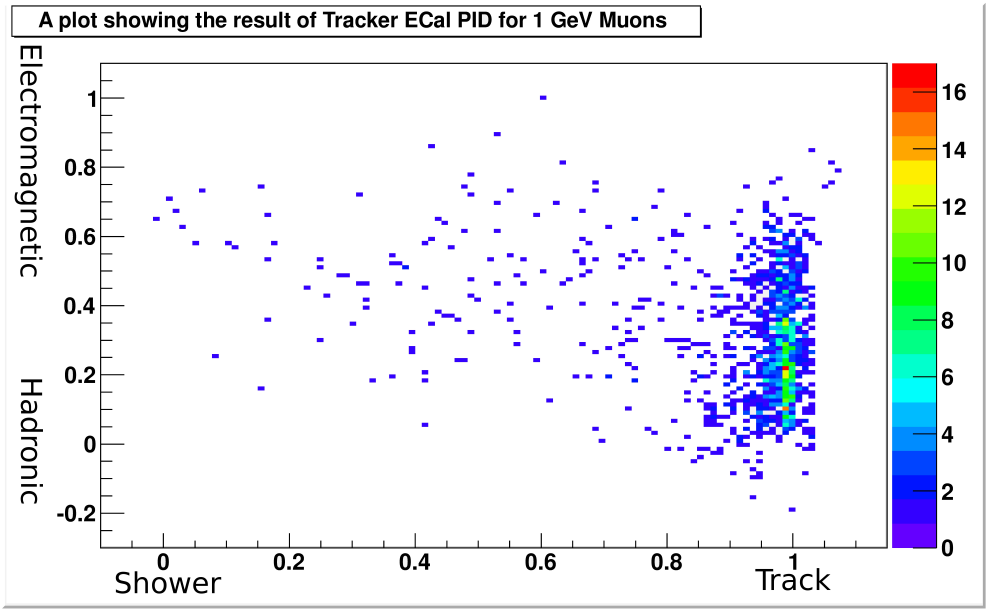

Fig. 4.14. This plot shows the PID output when run over 1500 simulated 1 GeV muons incident on the front face of the DsECal. Each muon is simulated with a random incident angle of up to 70 degrees from the beam axis. The 2D plot shows the output from both the Track vs Shower decision and the Electromagnet vs Hadronic decision. The PID decision clearly favours a track, which is consistent with a typical muon deposit.

All reconstruction packages in the ND280 software return objects defined by the software group as a whole. These are returned with the required parametrisation needed for 'global' reconstruction. This global reconstruction will in the future be done using the tool RECPACK (Cervera-Villanueva et al. (2004)).

4.2.5 Analysis Software

The ND280 software is designed to have a pure Root reduced data format, where the results of the reconstruction analysis are saved. This allows the analyser to have a standard and portable data file to study. With the global reconstruction and analysis module still in development, early analysis required a results module for each subdetector's reconstruction. The design of this was left to each reconstruction group. Similar to the last section, the calorimetry's module will be described in brief here to offer the reader an example and to highlight the author's work.

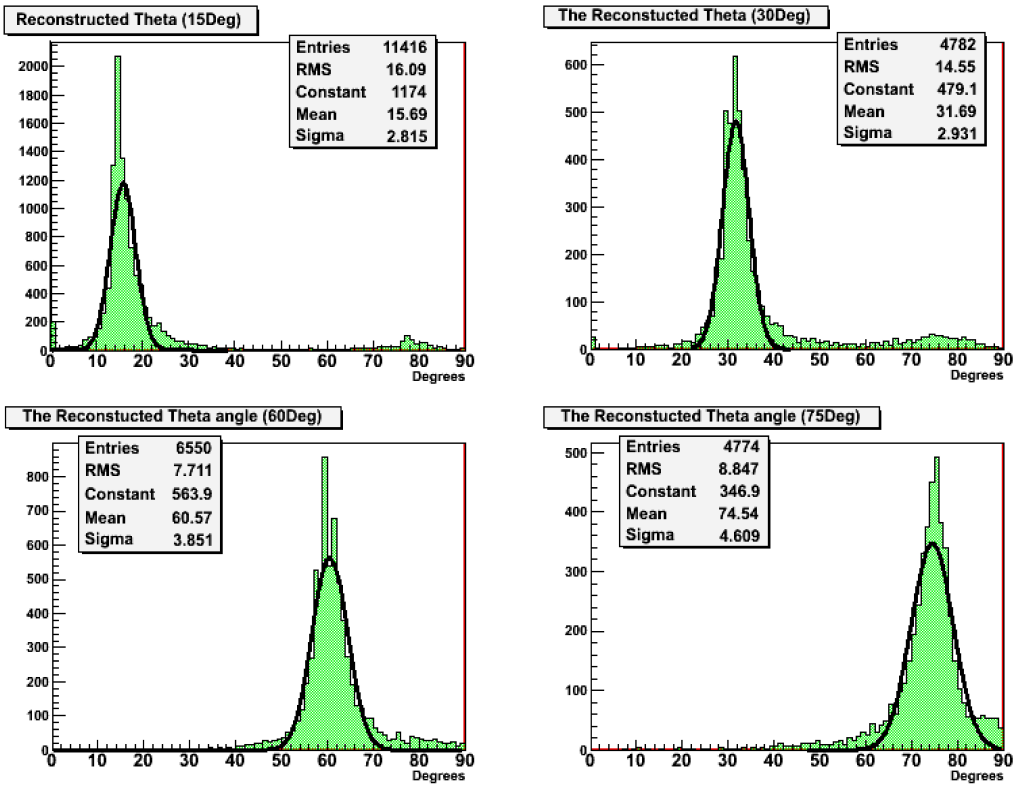

Fig. 4.15. This plot shows the ECal direction fitter for reconstructed tracks. The data used in these plots was taken at CERN as part of the DsECal commissioning. The ECal was placed at different angles in respect to a testbeam. For each configuration the testbeam data used was 600 MeV charged pions.

The design of this module follows a similar format to the oaEvent Recon Object structure. This conformity is designed to help the user in navigation. Each event with a fully reconstructed object is returned here as a ReconObject. The design structure is seen in full in figure 4.16

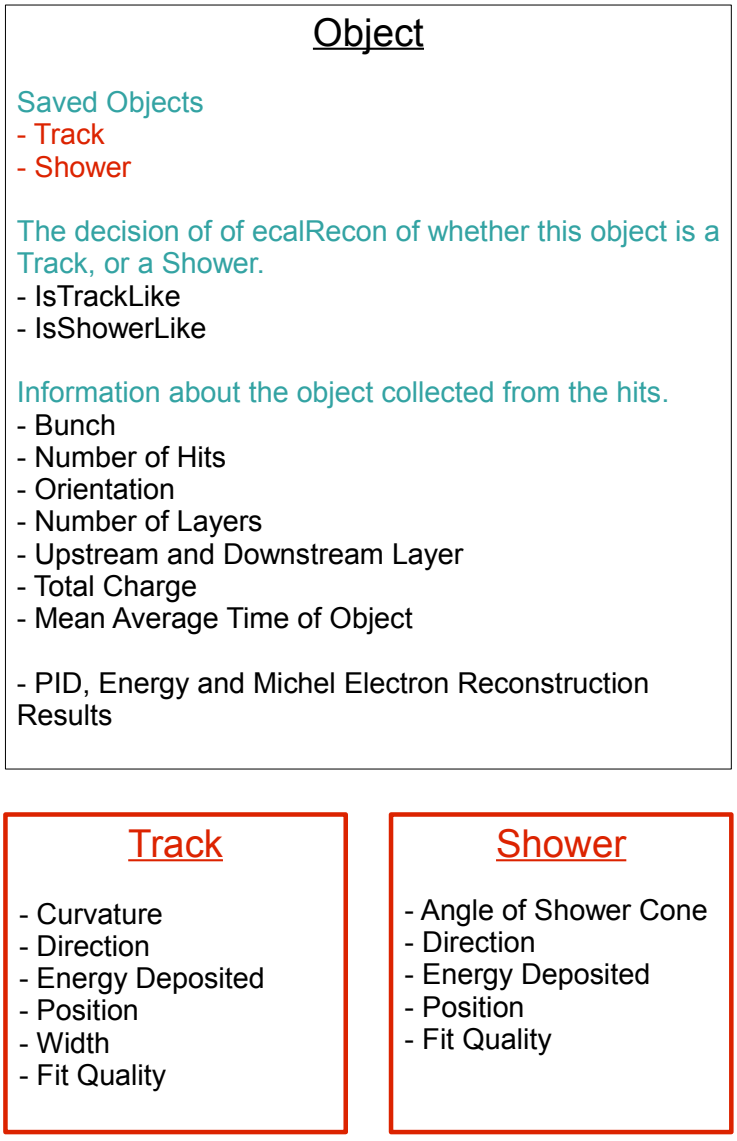

Fig. 4.16. The structure for an analysis tool that outputs useful reconstructed data calculated inside the Tracker ECal reconstruction software.

A feature important to note here is the inclusion of both Track and Shower fits. With all PID information also included, the module allows the Particle Identification decision to be made by the analyser rather than the reconstruction group.

Chapter 5

TrackFitter

5.1 Introduction and Aim

Before any data was taken, the ND280 detector went through a commissioning period. In this period the DsECal was installed together with all TPCs, FGDs, SMRDs and P0D Modules. With these detectors coming together for the first time, both the hardware and software involved in data taking was put under its biggest test. During the commissioning of the Downstream Calorimeter, there was a requirement for a simple and robust tool that could quickly reconstruct cosmic ray data into well understood tracks. These tracks would provide data needed in the tuning of calibration methods and also contribute to a pool of information used to track the progress of the ECal commissioning.

5.2 Method

The method of reconstruction was kept simple by design, enabling it to perform quickly when fast testing of new methods was important. It used the first stages of ECal hit reconstruction to provide basic 2D clusters, see section 4.2.4.3. These 2D clusters were collected with the tools described in chapter 4.2.4.

The track fitter then fits a straight line through these clusters. For a typical event there will be three or four straight line fits, one for each orientation and MPPC. The Barrel Calorimeters have three as one of their two bar orientations contains only single ended bars, meaning that only one end of the WLS fibre is connected to an MPPC and the other is mirrored. Whilst data collected in the DsECal provides four fits due to the two orientations of double ended bars. Discussion here will mainly concern data taken when the tool was created during the commissioning of the DsECal.

Before the fits were performed, early cuts were made to discard events that do not fit the typical minimum ionizing particle (MIP) like deposit needed when collecting only well understood cosmic candidates. To place these cuts in context, some features of the DsECal will be reviewed at this point. The detector has 34 layers, seventeen of each bar orientation. It stands

so that the normal to the detector planes was horizontal, therefore most cosmic rays were at a high angle θ, where θ is specified as the angle away from this normal. For additional interest, the trigger used when taking this data took a coincidence between sensor TFBs at the most downstream layers of the calorimeter.

The initial cuts to the clustered hits are:

- All views must have between two and twenty one hits. By limiting the number to 21 many showering objects which often contain many hits will be removed.
- The total number of hits in all views is cut tightly at thirty hits in total. This will again remove many showering objects that deposit energy in many bars in each layer.
- The track must span ten layers and have a clear entrance and exit location from the detector. This will ensure that only have through-going, well-understood MIP tracks are selected.

The last cut was altered to its current state after analysis of the primary data. When the fitter was first designed, only tracks that had hits in the first and last layer were used. However this was found to exclude too many objects when the ECal was 'stood up' to replicate its final positioning in the detector suite. It was therefore decided that the method would be expanded to collect tracks which entered or exited the detector from the top, bottom or sides. This was designed to assign an edge region to all ECal detectors and to make the cut without slowing down processing time. Monitoring how fast the fitter could perform was a constant in its development and study.

With the more obvious showering and undesirable tracks removed, fitting of the straight line path of the MIP could proceed. To perform the fit the ROOT Object (Brun & Rademakers (1997)) TF1 was used with TGraphErrors and fitted over its length. This method uses a least squares straight line fit which finds the minimum of the square of the residuals to a line fit. If the points of data are labeled $(x_1,y_1),(x_2,y_2),...(x_i,y_i)...(x_n,y_n)$, the fitted line $f(x_i) = mx_i + c$ has a residual r_i from from a point (x_i,y_i), where $r = y_i - f(x_i)$. The straight line parameters m and c are then found minimising the summed square of the residuals.

$$E(m,c) = \sum_{i=1}^{n} (y_i - (mx_i + c))^2 = Minimum \tag{5.1}$$

You can perform this minimisation arithmetically by taking the partial derivatives of E with respect to m and c and setting each to zero. ROOT however minimises this using Minuit (James (2006)). With the minimisation done, the fitted line can be constructed and a final set of cuts are made to remove hits that are not part of the straight track that the method is tasked to find.

All hits that lay outside a bar width (40 mm) from where the fit passed through the layer are cut. This process was added in order to remove outlying hits. The source of these hits could be Michel electrons or scattered objects but the exact reason for outlying hits was not investigated due to time constraints. With this cut made the line is refitted over the remaining points. This process of fitting and removal is repeated until no outlying hits are found. The process is illustrated in Figure 5.1.

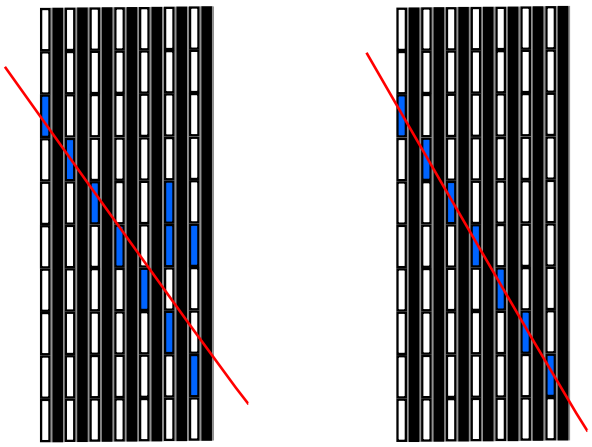

Fig. 5.1. This illustrates the fitting of a straight line before and after outliers are removed on a 2D projection of a section of the DsECal. Here the red line represents the fitted MIP track and the blue rectangles refer to the hit bars. On the left the clustered object has included a number of hits that have large residuals to the fitted line. These hits are then cut and a straight MIP track is returned as the result of the fitter.

The fitter returns all reconstructed objects that are made from a combination of at least three views with more than 9 hits in each. This last cut is a quality control cut and was put in place in order to restrict returned tracks to the straight well understood objects that were required by the calibration and commissioning groups.

5.3 Results

Figure 5.2 shows a typical straight line fit made by the tool, here all four two dimensional fits are shown. Figure 5.3 is also included and shows an event display of the fitted track from

figure 5.2. This image was included to highlight the use of the fitter as it shows an issue with the event display geometry at the time of testing. In the topmost image a straight track is seen in two locations. These simple tests made the fitter invaluable during this initial data taking stage in the detector's commissioning.

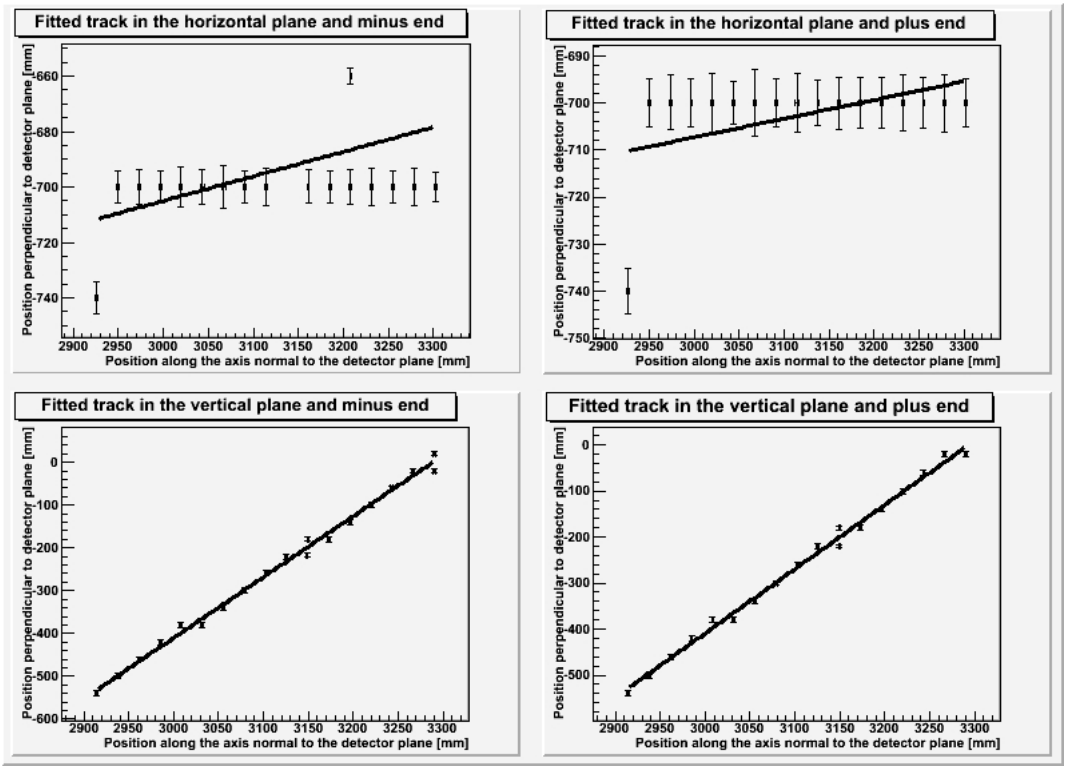

Fig. 5.2. The figure shows four straight line fits from a cosmic track passing through the Downstream ECal. Here the positive and negative ends refer to each of the bar's two sensors. This particular set of plots shows a typical cosmic track passing through the calorimeter whilst the detector was in its final position in the ND280 detector hall but without any magnetic field.

A MIP path in three dimensions is needed in order to monitor a variety of effects during commissioning. Two 2 dimensional fits in orthogonal views with the lowest χ^2 are then used to create a three dimensional path through the calorimeter. This fitter was used in a number of calibration tasks, for example it was the source of hits used when producing the normalisation constants needed to tune the response of each MPPC. It was also used throughout commissioning to perform confidence checks.

5.4 Highlighted uses of the Track Fitter

A short term study into triggering is included to illustrate the use of the track fitter.

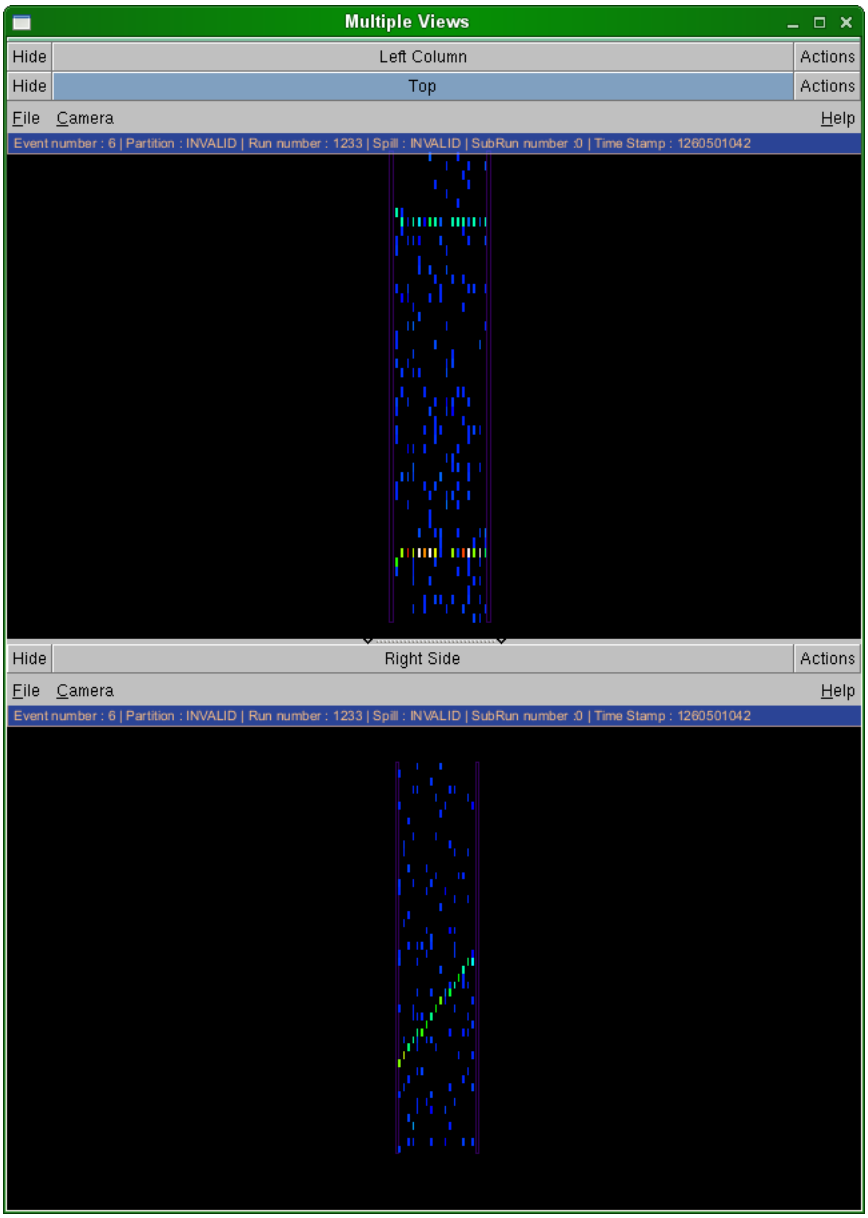

Fig. 5.3. Shown here is the corresponding event display of the fit shown in figure 5.2. It also indicates the ability of the fitter to highlight minor commissioning issues. The two tracks in the top view are not a real structure and occur due to some simple early issues with the geometry. These problems were quickly addressed once highlighted by the fitter.

5.4.1 DsECal and FGD Trigger Study

This study looked at the distribution of MIPs collected using two different trigger configurations. The DsECal, unlike other ECals in the ND280, is used as part of the ND280 cosmic trigger. The back DsECal layers are used with the SMRD and the front P0D Module to contain all ND280 modules with full triggering. This allows the recording of all objects entering and exiting the detector. Each sub-detector section of the trigger array can be used individually and this study makes use of the DsECal trigger. The trigger works by requiring a coincidence

between signals recorded in different TFBs in only the downstream layers of the ECal. Due to the cosmic muons oblique incident angles, many glancing MIP objects are expected to trigger the DsECal only triggering. In addition with the downstream trigger location, tracks leaving the detector in the upstream layers will be more common than those that deposited more energy in the upstream layer and exit in the downstream section, see figure 5.4.

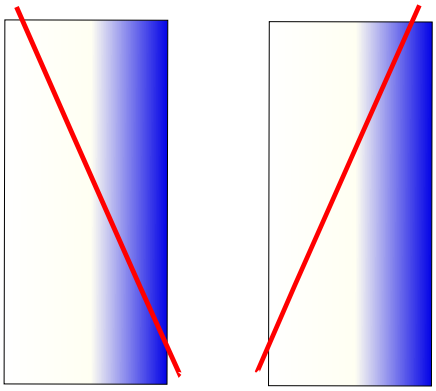

Fig. 5.4. The drawing here illustrates that tracks entering from the left or upstream side of the detector will deposit more energy as their path travels through the detector.

The DsECal only trigger will be compared to another trigger configuration. This second trigger is set up using the two FGDs which sit further upstream in the ND280 basket from the studied DsECal. When a MIP track is seen in both FGDs, the trigger will fire and record this object. The Tracks recorded by the FGD trigger are therefore much more horizontal than those seen with the DsECal only trigger. In addition the FGD trigger also provides much higher energy samples as lower energy cosmic rays travelling at this angle are more often absorbed or scattered by the increased amount of atmosphere they must traverse before arriving at the detector. Results from this study are included in figures 5.5, 5.6, 5.7 and 5.8. These plots clearly show the expected distribution discussed previously. They also highlight the usefulness of the track fitter and the quality of this commissioning tool.

5.5 Conclusion

The fitter was widely used during the Downstream ECal commissioning and was a tool designed for a very specific time in the production of the ND280. When concluding this work then it must be noted that it was designed not to reconstruct every track, but to reconstruct clean and well understood tracks as quickly and accurately as possible. If continued work on

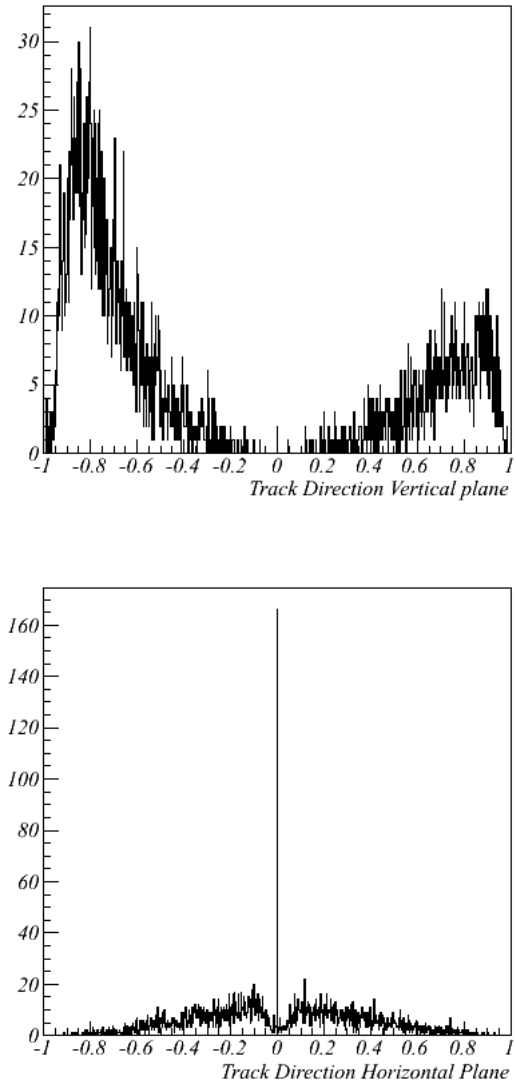

Fig. 5.5. Shown here are the reconstructed direction distributions of cosmic muons when using the DsECal only trigger. The directions shown here are given through a measure of the angle theta. Theta is the angle away the global z axis, defined as an angle perpendicular to the DsECal's face. This plot shows the high proportion of glancing muons incident on the DsECal which are detected using the DsECal only trigger. In addition, the track's predominantly upstream direction is also clear. The spike at 0 degrees occurs due to the granularity of the detector; all tracks that traverse the detector by passing through bars on the same level will be placed in this bin.

the package were possible I would have investigated a couple of additional areas. The biggest improvement could be made in how our two dimensional fits are matched into three dimensional tracks. The current method, which uses the two orthogonal tracks with the lowest χ^2, is crude and could be improved. The first step in improving this would be combining the two fits from similar bars. If this could be done quickly and simply, the fitter would show improvement in its ability to accurately find directions and positions of the cosmic tracks studied. I feel

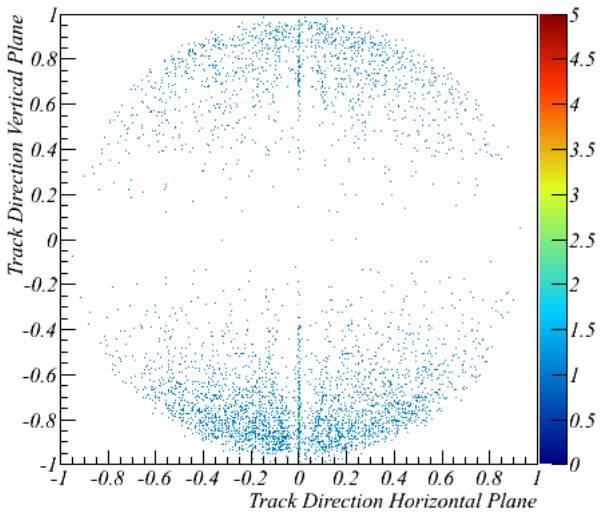

Fig. 5.6. This plot shows the 2D theta direction distribution with the DsECal only trigger. The directions shown here are given through a measure of the angle theta. Theta is the angle away the global z axis, defined as an angle perpendicular to the DsECal's face. This further illustrates the high number of glancing muons collected when using the DsECal only trigger. The banding seen in the centre of this plot is due to an artefact of early reconstruction.

that understanding more about the outlying hits that are cut during fitting would also be of benefit. Perhaps this would not be beneficial inside the original design remit but it could provide an interesting study. The ownership of the tool was passed on to another T2K student as my studies on other analysis became more time demanding. Currently the fitter is still used in calibration, however with the time restraints on data reconstruction during commissioning not in affect during regular detector running, the full reconstruction detailed in section 4.2.4 is now used for most analyses.

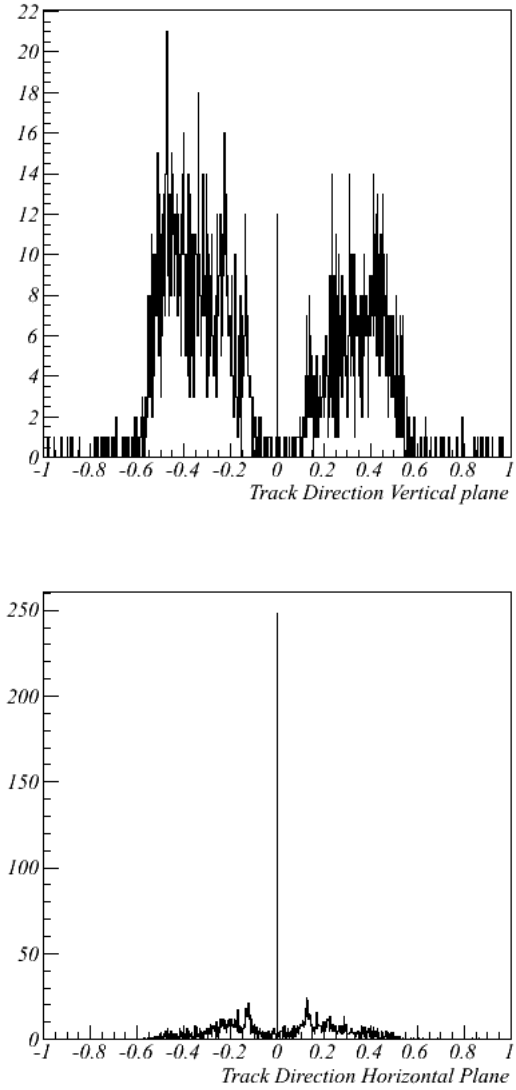

Fig. 5.7. Shown here are the reconstructed direction distributions of cosmic muons when using the FGD only trigger. The directions shown here are given through a measure of the angle theta. Theta is the angle away the global z axis, defined as an angle perpendicular to the DsECal's face. This plot clearly shows the higher proportion of low theta angle muons incident on the DsECal when using the FGD only trigger. The spike at 0 degrees occurs due to the granularity of the detector; all tracks that traverse the detector by passing through bars on the same level will be placed in this bin.

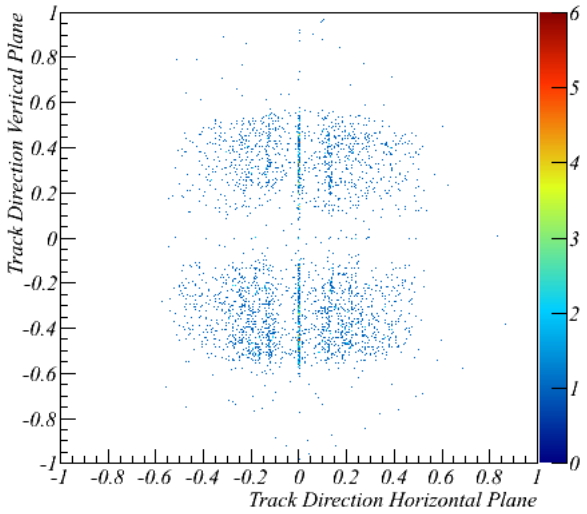

Fig. 5.8. This plot shows the 2D theta direction distribution with the FGD only trigger. The directions shown here are given through a measure of the angle theta. Theta is the angle away the global z axis, defined as an angle perpendicular to the DsECal's face. This further illustrates the higher number of low theta angle muons when using the FGD trigger. The banding seen in the centre of this plot is due to an artefact of early reconstruction

Chapter 6

CC1π^0 Analysis

Neutrinos can interact weakly through the exchange of a W boson with a target nucleon to produce a neutral pion and no other mesons; this interaction, discussed earlier in section 2.3.1, is the focus of the following study.

6.1 Analysis Aim and Motivation

The aim of this work is to find and study charged current neutrino interactions that produce one neutral pion; this interaction is also known as CC1π^0.

At the time this study took place (early 2010), the ND280 detector was still in its commissioning period. Most notably, the ECals around the TPC and FGD tracker region did not offer complete coverage. Two sections of the full ECal detector system were fitted, with only the DsECal fully operational. This is unfortunate as calorimetry is of high importance when studying π^0 interactions because it can be used to detect the photons produced from neutral pion decay.

The motivation to study such a channel goes beyond general interest and the measurement of an interaction which is poorly understood at this energy scale. The CC1π^0 interaction produces a charged lepton as well as the neutral pion. The composition of the ν_μ T2K beam means that the charged lepton produced is most commonly a muon. This muon leaves an ionised track which can be well reconstructed from its point of creation (vertex) with the neutral pion. The channel then presents a good opportunity to study neutral pion production, with an easily reconstructed vertex location. This provides a well understood set of events to test neutral current pion NC1π^0 reconstruction methods. NC1π^0 is a channel which is difficult to reconstruct and additionally it is a specific background to ν_e appearance measurements at Super-Kamiokande. The known vertex location can also provide data that could help with tuning of the energy scale during the early stages of data collection and detector commissioning.

6.2 Channel Signature and Acceptance Study

Shown in figure 6.1 is an example of a simulated CC1π^0 event. The event highlights the signature of the channel (see section 2.3.1).

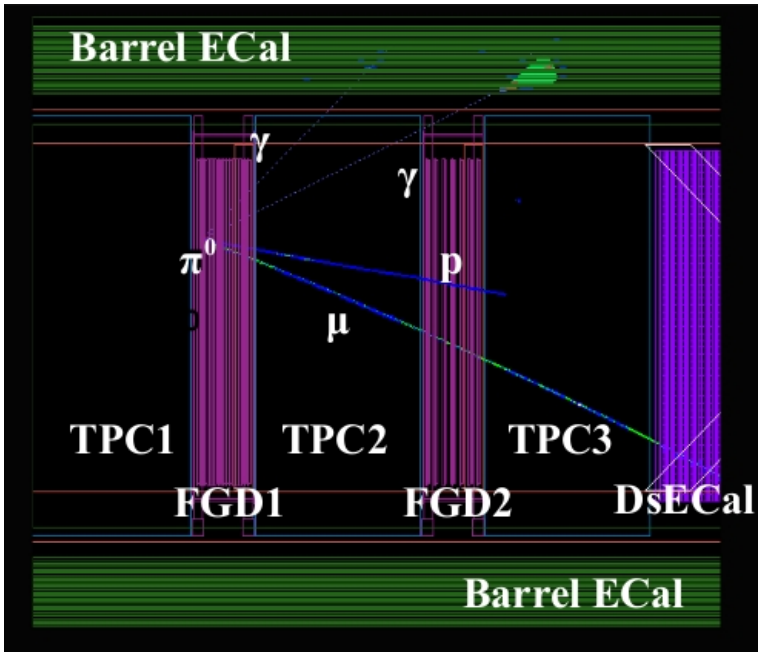

Fig. 6.1. An event display of a typical CC1π^0 event which is highlighted by one muon track, two photon showers and a nucleonic track.

In order to investigate the signal topology in the tracker region, an acceptance study was performed. In the study 6428 CC1π^0 Monte Carlo events were created in the FGDs, the equivalent of approximately 4.5 $\times$ 10^{20} protons projected onto the T2K target. In comparison, the data collected during the first data taking period corresponds to 3 x 10^{19} protons on target.

Muons produced in the interaction are typically highly boosted in the beam direction, as shown in figure 6.2.

This means that the majority of muons will pass through neighbouring TPCs allowing good muon momentum reconstruction.

Photons produced in the π^0 decay present a number of issues. Due to the typically low energy π^0 produced, the photon directions appear close to isotropic. This can be seen in figure 6.3.

This presents a problem for the study when combined with the limited ECal coverage available at the time of analysis. To compound this issue many of the photons are created with

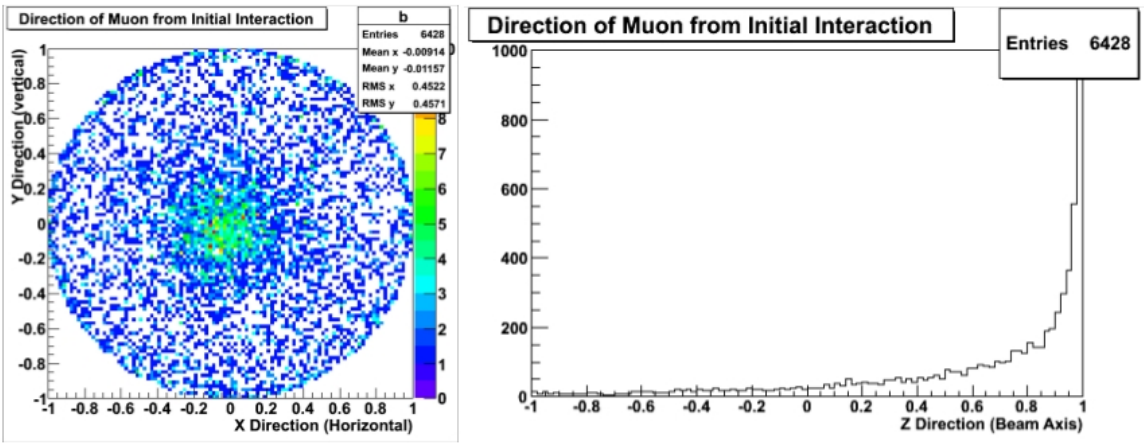

Fig. 6.2. These plots show the direction of muons produced in CC1π^0 interactions in the ND280 detector. The plot on the right describes the muon direction plotted as cosθ away from the beam angle.

very low energy (see figure 6.3). This study found that approximately 20% of the photons convert before reaching the ECals, producing low energy electron positron pairs. This produces a challenging energy and direction reconstruction problem. Any photons that do reach the ECals have energies close to the 50 MeV minimum resolution limit of the ND280 calorimetry. This further limits direction and energy reconstruction.

6.3 Early Event Selection

The early selection detailed here looks for π^0 events in the Monte Carlo data created for the acceptance study. Section 6.2 highlighted a number of challenges to this study yielding meaningful results at the stage in software development and detector commissioning during which the author worked on the experiment. The aim of this selection study is to determine the feasibility for a full data selection.

The selection results can be seen in Table 6.1

Cuts	Number Of Events	Percentage of Events Remaining
True Vertex in the FGD Fiducial	2903	100
Reconstructed Vertex in the FGD	1509	52
Negative Track in the TPC	932	32
Two ECal Showers in time	154	5

Table 6.1. Table to show the cuts used in a CC1π^0 selection. Data used was a full detector Monte Carlo simulation filtered to select purely CC1π^0 events.

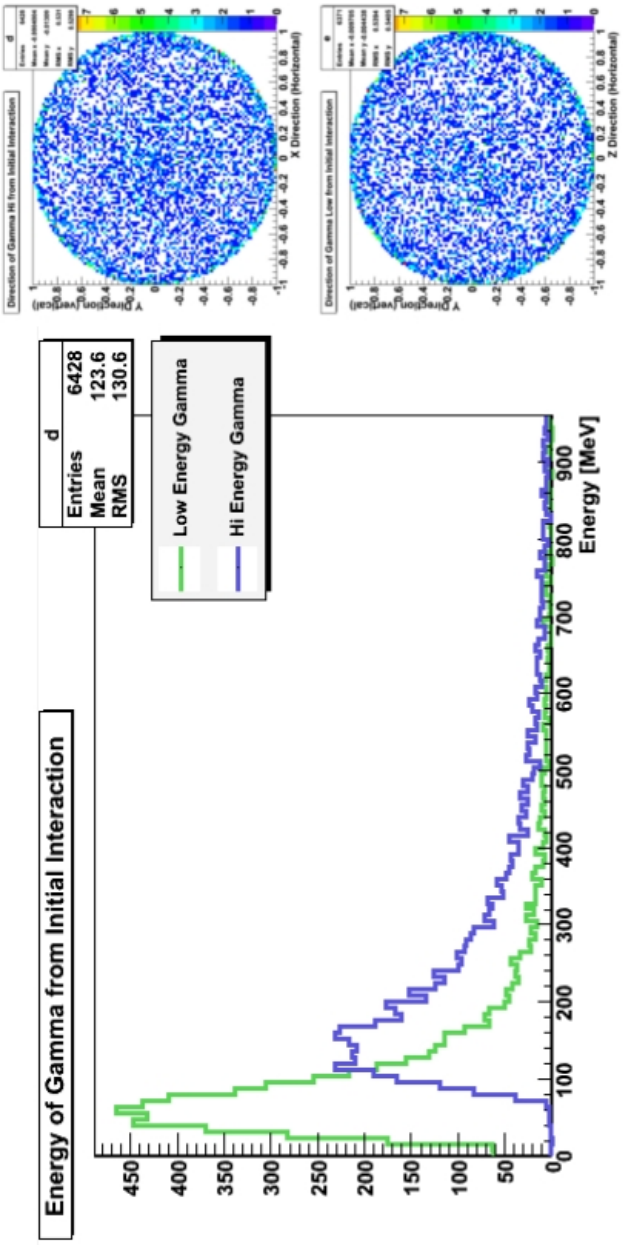

Fig. 6.3. Plots to show the energy and directional profile of photons created in π^0 decay

The first cut looks for true vertices in the FGD fiducial volume. This was put in place in order to obtain a pure sample of π^0 interactions that should then be collected by the selection. The FGD's vertex finder reconstructs 52% of the vertices inside the FGD and a further 20% of events are lost when looking for a negative track in the TPC. The final cut removes all but 5% of the available events when looking for two showers contained in the DsECal.

Using the remaining 154 events, an invariant mass distribution of the photon pair was made using the reconstructed photon shower energies and direction. The two photon invariant mass $m_{\gamma\gamma}$ is given by

$$m_{\gamma\gamma}^2 = 2E_1E_2(1-\cos(\theta)) \tag{6.1}$$

where E_1 and E_2 are the two photons produced from the decay of the π^0, and θ is the angle between them.

The invariant mass distributions are shown in figure 6.4

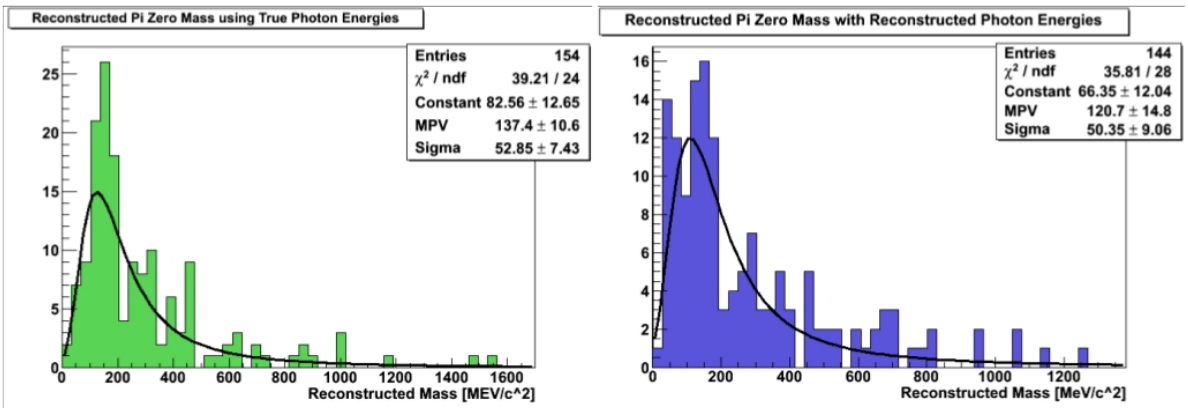

Fig. 6.4. Plots to show a comparison of calculations of the $\gamma\gamma$ invariant mass. The left plot uses energies given by the Monte Carlo simulation, whilst the right plot shows energies reconstructed using simulated electronics response.

This highlights the importance of well understood photons in the accuracy of π^0 reconstruction and concludes the work done on this channel by the author.

6.4 Conclusion

This study investigated the charged current single neutral pion channel and its reconstruction in the tracker region of the ND280 detector. The study was performed through investigation

of simulated data which had been created using the ND280 software and the GENIE neutrino interaction generator (see chapter 4). The simulated detector mimics the then incomplete ND280 detector at the time of the study. Most notably at this point, the DsECal was included as the only working calorimetry for the tracker region. The simulated data used corresponds to approximately ten times the protons on target that had been delivered before the summer shut-down in 2010. This marked the end of the period of study described in this thesis.

It was found that with simple cuts, even with 100% purity, you would expect to reconstruct approximately 15 π^0 events during the aforementioned period of study. Based on this and knowledge of the current reconstruction packages, it was concluded that reconstructing these 15 events in real data would have been impractical. The limitations contributing to the low number of events that could be resolved were many, but reconstruction of photons produced in the π^0 decay can be highlighted as a particular issue. With only one calorimeter functioning, the coverage for almost isotropically produced photons was a key issue and one that would only be resolved when all remaining calorimeters were commissioned and installed in 2011. The other key challenge for this channel is that many of the photons produced do not reach the calorimetry before converting into a e^+e^- pair.

Positives can be found in the study also. The reconstructed energy and shower directions for each photon produced promising measurements for the invariant mass of the neutral pion. The FGD and TPC reconstruction also showed promise when reconstructing this challenging channel during early commissioning.

Chapter 7

Conclusion

This thesis describes some of the projects within the T2K collaboration that the author was part of between summer 2007 and the end of 2010. Much of this work involved the calorimetry for the Tracker region in the T2K near detector (ND280). The first Tracker electromagnetic calorimeter was structurally completed in the beginning of 2009 at Lancaster University. This detector was designed to be the downstream calorimeter within the ND280 detector. Both the near and far detectors used in the T2K experiment were discussed in this thesis, with special note given to the construction of the downstream calorimeter. After structural completion, the downstream calorimeter went through six months of testing and early commissioning. This process started in the UK before progressing onto CERN in summer 2009, where the T2K UK group made use of the T7 test beam.

Throughout this period, design and implementation of the modelling, calibration and reconstruction software for the ND280 detector had been taking place. The test beam at CERN provided an early opportunity for testing of this software. A review of event reconstruction in the calorimeter was given in this thesis with much of this review performed on a version of the software completed in early 2010. This review showed promising resolutions for energy reconstruction, PID, and position and direction reconstruction. Improvements in the software at this time were coming through the integration of time based cuts performed when clustering hits together, which had a positive effect on many of the later reconstruction stages. Future improvements in this work were to come from matching reconstructed objects in other areas of the ND280 with those within the calorimetry. Information obtained in other specialised subdetectors would provide benefits for a number of the algorithms with the calorimetry, most notably the particle identification.

The detector was then moved to its final position within the ND280 at J-PARC in the autumn of 2009. Commissioning of the detector revealed a requirement for a fast and efficient source of reconstructed straight cosmic sourced MIP tracks. This role was fulfilled by a track fitter developed by the author in early 2010, which allowed for study of detector triggers, as well as providing a source of understood objects for calibration tools. The fitter was designed to

run quickly rather than with high resolutions. Therefore improvements may come in the future through the utility it provides. It would be of benefit to the user to have a method to tune the fitter in order to provide objects with specified requirements. This could be objects entering with set angles or from certain entry positions.

The neutrino induced charged current single neutral pion study was an early project which would make use of the calorimetry reconstruction. The study focused on looking for neutrino vertices in the fine grain detectors in the ND280 tracker region. The neutral pions targeted in this study typically decay into two photons. Reconstruction of the energy and direction of these photons allows for the reconstruction of the parent invariant mass. The conclusion of this study was that, due to both the low number of events and an incomplete detector set-up, a study using real events was unrealistic at the time. With the current full detector set-up, larger statistics and further reconstruction improvements available, an efficient selection of CC1π^0 may now be possible.

Bibliography

Abdurashitov, J. et al. (2009) Measurement of the solar neutrino capture rate with gallium metal. III: Results for the 2002–2007 data-taking period. Phys.Rev. C80:015807.

Abe, K. et al. (2011a) Indication of Electron Neutrino Appearance from an Accelerator-produced Off-axis Muon Neutrino Beam. Phys.Rev.Lett. 107:041801.

Abe, K. et al. (2011b) Search for Differences in Oscillation Parameters for Atmospheric Neutrinos and Antineutrinos at Super-Kamiokande. Phys.Rev.Lett. 107:241801.

Abe, K. et al. (2011c) The T2K Experiment. Nucl.Instrum.Meth. A659:106–135.

Abgrall, N. et al. (2011) Time Projection Chambers for the T2K Near Detectors. Nucl.Instrum.Meth. A637:25–46.

Adamson, P. et al. (2011) Measurement of the neutrino mass splitting and flavor mixing by MINOS. Phys.Rev.Lett. 106:181801.

Agostinelli, S. et al. (2003) GEANT4 A Simulation Toolkit. Nuclear Instruments and Methods A505:250–303.

Aharmim, B. et al. (2008) An Independent Measurement of the Total Active B-8 Solar Neutrino Flux Using an Array of He-3 Proportional Counters at the Sudbury Neutrino Observatory. Phys.Rev.Lett. 101:111301.

Aharmim, B. et al. (2010) Low Energy Threshold Analysis of the Phase I and Phase II Data Sets of the Sudbury Neutrino Observatory. Phys.Rev. C81:055504.

Andreopoulos, C., Bell, A., Bhattacharya, D., Cavanna, F., Dobson, J. et al. (2010) The GENIE Neutrino Monte Carlo Generator. Nucl.Instrum.Meth. A614:87–104.

Apollonio, M. et al. (2003) Search for neutrino oscillations on a long baseline at the CHOOZ nuclear power station. Eur.Phys.J. C27:331–374.

Arpesella, C. et al. (2008) Direct Measurement of the Be-7 Solar Neutrino Flux with 192 Days of Borexino Data. Phys.Rev.Lett. 101:091302.

Bahcall, J. N. & Davis, R. J. (1976) Solar Neutrinos: a scientific puzzle. Science 191:264–267.

Barabash, A. (2011) Double Beta Decay: Historical Review of 75 Years of Research. Phys.Atom.Nucl. 74:603–613.

Beavis, D., Carroll, A., Chiang, I. et al. (1995) Long Baseline Neutrino Oscillation Experiment at AGS (Proposal E889). Physics Design Report, BNL, 52459 .

Beringer, J. et al. (2012) The Review of Particle Physics. Phys. Rev. D86:010001. See also http://pdg.lbl.gov.

Brun, R. & Rademakers, F. (1997) ROOT: An Object Oriented Data Analysis Framework. Nucl. Inst. Meth. A389:81–86. See also http://root.cern.ch.

Carver, A. (2010) Electron identification in and performance of the ND280 Calorimeter .

Cervera-Villanueva, A., Gomez-Cadenas, J. & Hernando, J. (2004) 'RecPack' a reconstruction toolkit. Nucl.Instrum.Meth. A534:180–183.

Chadwick, J. (1932) Possible Existence of a Neutron. Nature 129:312.

Cleveland, B., Daily, T., Davis, Raymond, J., Distel, J. R., Lande, K. et al. (1998) Measurement of the solar electron neutrino flux with the Homestake chlorine detector. Astrophys.J. 496:505–526.

Cowan, C. L. J., Reines, F., Harrison, F. B., Kruse, H. W. & McGuire, A. D. (1956) Detection of the Free Neutrino: a Confirmation. Science 124:103.

Danby, G., Gaillard, J., Goulianos, K. A., Lederman, L., Mistry, N. B. et al. (1962) Observation of High-Energy Neutrino Reactions and the Existence of Two Kinds of Neutrinos. Phys.Rev.Lett. 9:36–44.

Davies, G. (2011) Understanding and Calibrating the DsECal for T2K's ND280 .

Duck, I. & Sudarshan, E. C. G. (1997) Pauli And The Spin-Statistics Theorem. World Scientific Publishing Co. Pte. Ltd., Singapore.

Feldman, G., Hartnell, J. & Kobayashi, T. (2013) A Review of Long-baseline Neutrino Oscillation Experiments. Advances in High Energy Physics 2013. Article ID 475749.

Fermi, E. (1934) Trends to a Theory of beta Radiation (in Italian). Nuovo Cim. 11:1–19.

Fukuda, Y., Hayakawa, T., Ichihara, E., Ishitsuka, M., Itow, Y. et al. (2003) The Super-Kamiokande detector. Nucl.Instrum.Meth. A501:418–462.

Gando, W. et al. (2011) Constraints on θ_{13} from A Three-Flavor Oscillation Analysis of Reactor Antineutrinos at KamLAND. Phys. Rev. D 83:052002.

Giomataris, I., De Oliveira, R., Andriamonje, S., Aune, S., Charpak, G. et al. (2006) Micromegas in a bulk. Nucl.Instrum.Meth. A560:405–408.

Glashow, S., Iliopoulos, J. & Maiani, L. (1970) Weak Interactions with Lepton-Hadron Symmetry. Phys.Rev. D2:1285–1292.

Hayato, Y. (2009) A neutrino interaction simulation program library NEUT. Acta Physica Polonica B 40:2477.

Hernandez, E., Nieves, J., Valverde, M. & Vicente Vacas, M. (2010) N-Delta(1232) axial form factors from weak pion production. Phys. Rev. D81:085046.

Hirata, K. et al. (1987) Observation of a Neutrino Burst from the Supernova SN 1987a. Phys.Rev.Lett. 58:1490–1493.

Hoecker, A., Speckmayer, P., Stelzer, J., Therhaag, J., von Toerne, E. & Voss, H. (2007) TMVA: Toolkit for Multivariate Data Analysis. PoS ACAT:040.

Hosaka, J. et al. (2006) Solar neutrino measurements in super-Kamiokande-I. Phys.Rev. D73:112001.

Hoshino, K. (2000) Result from DONUT: First direct evidence for tau- neutrino. pp. 58–63. Prepared for 8th Asia Pacific Physics Conference (APPC 2000), Taipei, Taiwan, 7-10 Aug 2000.

IRFU (2013) Images taken from the IRFU website. http://irfu.cea.fr/Sap/Phocea/Vie_des_labos/Ast/alltec.php?id_

James, F. (2006) Minuit: Function Minimiser. http://lcgapp.cern.ch/project/cls/work-packages/mathlibs/minuit/index.html.

Jolliffe, I. T. (1986) Principal Components Analysis. Springer-Verlag, New York.

Kavraki, L. E. (2007) Dimensionality Reduction Methods for Molecular Motion, Connexions Website. http://cnx.org/content/m11461/latest/.

Kayser, B. (2004) Neutrino physics. eConf C040802:L004.

Litchfield, R. P. (2012) (Direct) Measurement of theta-13. Invited talk at Flavor Physics and CP Violation (FPCP 2012), Hefei, China, May 21-25, 2012.

Mikheev, S. P. & Smirnov, A. Y. (1986) Resonant amplification of neutrino oscillations in matter and solar neutrino spectroscopy. Nuovo Cim. C9:17–26.

Nobelprize.org (2012) The nobel prize in physics 1979 http://nobelprize.org/nobel_prizes/physics/laureates/1979/.

Nobelprize.org (2013) Press release: The 1995 nobel prize in physics. http://www.nobelprize.org/nobel_prizes/physics/laureates/1995/press.html.

Pauli, W. (1930) Pauli letter collection: Letter to lisa meitner. http://cds.cern.ch/record/83282/files/meitner_0393.pdf.

Pauli, W. (1940) The Connection Between Spin and Statistics. Phys. Rev. 59:716–722.

Ritt, S., Amaudruz, P. & Olchanski, K. (2013) MIDAS (Maximum Integration Data Acquisition System) Wiki. https://midas.triumf.ca/MidasWiki/index.php/Main_Page.

Rutherford, E. (1920) Bakerian Lecture. Nuclear Constitution of Atoms. Proc. R. Soc. Lond. A July 1, 1920 97 686 374-400 .

Stodolsky, L. (1998) The Unnecessary wave packet. Phys.Rev. D58:036006.

T2K (2013) T2K Official Documents: Photographs and Figures. http://www.t2k.org/docs/photos/general.

Uhlenbeck, G. E. & Goudsmit, S. (1925) Die Naturwissenschaften 47:953.

Vacheret, A., Barker, G., Dziewiecki, M., Guzowski, P., Haigh, M. et al. (2011) Characterization and Simulation of the Response of Multi Pixel Photon Counters to Low Light Levels. Nucl.Instrum.Meth. A656:69–83.

Wikipedia (2011) Diagram of Particles Discovered in the Standard Model. http://en.wikipedia.org/wiki/Electron.

Wolfenstein, L. (1978) Neutrino oscillations in matter. Phys. Rev. D17:2369–2374.

Yamazaki, Y. et al. (2003) Accelerator Technical Design Report for J-PARC. hadron.kek.jp/ãccelerator/TDA/tdr2003/index2.html.

Zeller, G. (2008) Low energy neutrino cross sections from K2K, MiniBooNE, SciBooNE, and MINERvA. J.Phys.Conf.Ser. 136:022028.